Combined antagonism of Oncostatin M (OSM) and Interleukin 6 (IL-6) provides both anti-fibrotic and anti-inflammatory benefit in pulmonary fibrosis

Rojo A. Ratsimandresy[1], Emma Doran[1], Hart S. Dengler[1], Sarah E. Headland[1], Christopher J. Wedeles[1], Riccardo Guidi[1], Daqi Xu[1], Jiatong Liu[2], Yongchang Shi[3], Jianyong Wang[3], Salil Uttarwar[4], Alexander R. Abbas[4], Tianhe Sun[1], Daryle J. DePianto[1], Katrina B. Morshead[1], Joe Arron[1], Jason R. Rock[1], Jack Bevers 3rd [5], Rajbharan Yadav [6], Thirumalai Ramalingam[7], Xia Gao[7], Hans D. Brightbill[8], Claire L. Emson[8], Surinder Jeet[8], Alexander Arlantico[8], Aaron Wong[8], Sherman Yu[8], Tiffany Hao Tran[9], Laurie Leong[9], Monika Dohse[9], Cary Austin[9], Patrick Caplazi[9], Reynold A. Panettieri Jr.[10], Cynthia Koziol-White[10], William F. Jester Jr.[10], Andrey Shaw[11], Shimrit Avraham[11], Hari Menon[12], Spyros Darmanis[12], Zora Modrusan[12], Kimberly Kajihara[13], Masakazu Kanamori[14], Hideaki Shimada[14], Nathaniel R. West[11], Gerald Nakamura[5], Jason A. Vander Heiden[1,15*], Mark S. Wilson[1*$].

[1] Immunology Discovery, Genentech, South San Francisco, California 94080, USA,
[2] School of Medicine and Dentistry, University of Rochester Medical Centre, Rochester, New York, 14642, USA.
[3] Biochemical and Cellular Pharmacology, Genentech, South San Francisco, California, 94080, USA
[4] OMNI Bioinformatics, Genentech, South San Francisco, California 94080, USA,
[5] Antibody Engineering, Genentech, South San Francisco, California 94080, USA.
[6] Preclinical and Translational Pharmacokinetics and Pharmacodynamics, Genentech, South San Francisco, California 94080, USA,
[7] Biomarker Discovery, Genentech, South San Francisco, California 94080, USA,
[8] Translational Immunology, Genentech, South San Francisco, California 94080, USA,
[9] Pathology, Genentech, South San Francisco, California 94080, USA,
[10] Institute for Translational Medicine and Science, Rutgers, The State University of New Jersey, New Brunswick, NJ, 08901 USA
[11] Discovery Oncology, Genentech, South San Francisco, California 94080, USA,

32 [12] Next Generation Sequencing and Microchemistry, Proteomics and Lipidomics,
33 Genentech, South San Francisco, California 94080, USA,
34 [13] Infectious Disease, Genentech, South San Francisco, California 94080, USA,
35 [14] Chugai Pharmabody Research Pte. Ltd., Singapore
36 [15] Biological Research AI Development, Genentech, South San Francisco, California
37 94080, USA,
38 [$] Current position. Amgen Inc., South San Francisco. CA. 94080
39
40 * Lead contacts and correspondence to:
41 Mark S. Wilson, Ph.D, mwilso06@amgen.com,
42 Jason A. Vander Heiden, vanderheiden.jason@gene.com

Abstract

Interstitial lung diseases (ILDs), including idiopathic pulmonary fibrosis (IPF) and systemic sclerosis-associated ILD (SSc-ILD), are irreversible fibrosing diseases with a mean survival time of less than 5 years for IPF. Poorly understood etiology and complex pathogenesis of these diseases have hampered the identification and development of effective therapeutics. Existing treatments can slow progressive fibrosis and lung function decline but do not stop it entirely, resulting in a minimal impact on patient survival. Thus, novel therapeutic interventions are needed. Tocilizumab, an anti–IL-6 receptor antibody, was recently approved by FDA for the treatment of SSc-ILD based on evidence demonstrating a reduction in the rate of lung function decline. In this study, we have characterized an IL-6-driven feed-forward myeloid axis contributing to lung inflammation providing a mechanistic hypothesis for tocilizumab. Concomitantly we have identified an oncostatin M (OSM) orchestrated lung injury response contributing to epithelial and endothelial cell disruption, myofibroblast activation and fibrosis. Despite dysregulated expression of *IL11* in IPF, SSc-ILD, and murine models of fibrosis, we found no evidence for a pro-fibrotic role for IL-11 *in vitro* or *in vivo*. Instead, in pre-clinical models of IPF we demonstrate that antagonism of OSM alone, or to a greater degree in combination with IL-6, reduced lung fibrosis and inflammation. Translating these observations, we validated gp130:OSMR, rather than gp130:LIFR, as the dominant human receptor complex used by OSM, identifying OSMR as a potential therapeutic target to stall fibrosis.

Introduction

Interstitial lung diseases (ILDs), including idiopathic pulmonary fibrosis (IPF) and systemic sclerosis-associated ILD (SSc-ILD), are chronic, irreversible and often fatal pulmonary diseases that can carry an average prognosis of less than 5yrs[1-3]. IPF and up to 80% of SSc patients[4] present with pulmonary inflammation, vascular dysfunction, accumulation of subpleural fibroblasts and progressive fibrosis. Despite a good understanding of the pathophysiology of ILDs, there are very few treatment options available. Many prognostic biomarkers have been identified, including interleukin 6 (IL-6). Serum levels of IL-6 are elevated in patients with IPF and SSc and are predictive of lung function decline[5]. Experimental data support a pathogenic role for IL-6 with deletion of *Il6* or blocking the IL-6 pathway with monoclonal antibodies (mAbs) protecting mice from bleomycin (BLM)-induced lung and skin fibrosis, although the mechanism of protection has not been fully elucidated[6-8]. These observations spurred the clinical investigation of IL-6 in pulmonary fibrosis using tocilizumab (TCZ), a humanized monoclonal antibody directed against IL-6R that inhibits IL-6 signaling and previously approved for the treatment of rheumatoid arthritis, juvenile idiopathic arthritis, and giant cell arteritis[9]. Phase II (FaSScinate) and III (FocuSSced) clinical trials in patients with SSc found significantly fewer patients in the TCZ arm experienced a decline in lung function over 48 weeks of treatment, compared to placebo[10,11]. In 2019, TCZ was approved by the FDA for the treatment of SSc-ILD; however, these studies did not meet their primary endpoints of reducing skin fibrosis[10,11]. To date, pirfenidone, nintedanib, and nerondomilast are the only approved antifibrotic therapies for ILD's to slow pulmonary function decline[12,13], but they have well-characterized tolerability concerns and only moderately improve patient survival[14,15],thus leaving a need for more effective therapeutic options to prevent progressive fibrosis and improve patient outcomes.

Several profibrotic mediators have been described, including growth factors (CTGF, TGFβ family members), cytokines (IL-13 and IL-11), integrins, and vasoactive peptides[16]. In addition to these, oncostatin M (OSM) has long been associated with fibrosis[17-19] and is elevated in the bronchoalveolar lavage (BAL) fluid of SSc-ILD and IPF patients[20]. In pre-clinical studies, elevated OSM has accompanied fibrosis in a variety of

96 organs[21,22] and can induce fibrotic responses when exogenously delivered or over-
97 expressed in mice[20,23-28]. OSM-driven fibrosis appears to be independent of RAG-
98 dependent T and B cells, cKIT-expressing mast cells and basophils, STAT6[26] and IL-4R-
99 dependent IL-4 and IL-13 or TGFβ family members[20], suggesting a non-overlapping and
100 independent OSM-mediated mechanism of fibrosis. Despite these studies indicating
101 that OSM is sufficient to drive fibrosis, the role of OSM in pulmonary fibrosis and the
102 benefit of antagonizing OSM in pre-clinical or clinical settings is currently unclear.
103
104 Here we describe a mechanism of how IL-6 contributes to pulmonary fibrosis, identify a
105 critical role for OSM contributing to fibrosis, and demonstrate how antagonism of OSM
106 alone, or combined with IL-6, can provide therapeutic benefit. Specifically, we show
107 that IL-6 promotes the recruitment of a $CD64^+$ monocyte-derived macrophage
108 population, providing a mechanistic explanation for the benefit observed with IL-6R
109 antagonism in the clinic.
110
111 IL-6 signals through a heterodimeric receptor complex composed of IL6Rα and gp130.
112 Several other cytokines that have been implicated as mediators of pathological fibrosis,
113 including IL-11 and OSM, also use gp130 as a coreceptor. With the aim of identifying
114 pro-fibrotic mediators that can be targeted to stall progressive fibrosis we initially
115 assessed the contribution of IL-11 and OSM. We did not find any evidence that IL-11
116 contributes to pulmonary, kidney or liver fibrosis and instead identified a non-
117 redundant and critical role for OSM. Furthermore, IL-6 and OSM contribute in a non-
118 overlapping manner, with combined antagonism of IL-6 and OSM providing superior
119 protection from lung injury, inflammation and fibrosis. Translating these observations
120 to human systems, we identify *OSMR* expressing fibroblasts, epithelial, and endothelial
121 cells in both murine and human IPF lung tissue, characterize OSM-driven signaling,
122 transcriptional and physiological responses in all three primary human cell types, and
123 support OSMR as a viable therapeutic target to prevent progressive fibrosis.

124 # Results

125 **IL-6 drives CD64$^+$ macrophage activation in murine models of pulmonary**
126 **inflammation and fibrosis.**

127 We have clinically validated an important role for IL-6 signaling in lung function
128 decline in patients with SSc-ILD[11], however, IL-6R antagonism only partially impacted
129 fibrosis endpoints and fibrosis-related biomarkers. To better understand the
130 mechanisms of IL-6, we first investigated the role of IL-6 in the murine bleomycin
131 (BLM)-induced lung injury, inflammation, and fibrosis model. Confirming previous
132 reports of antagonizing this pathway [6-8], *Il6r*$^{-/-}$ mice had reduced lung injury and
133 inflammation at both day 8 and day 24 post-BLM (**Fig. 1a**) with reduced total
134 hydroxyproline, an amino acid necessary for collagen biosynthesis (**Fig. 1b**), along with
135 reduced *Col1a1* and *Col1a2* gene expression in lung tissue (**Fig. 1c**). Correlating with
136 reduced disease in *Il6r*$^{-/-}$ mice was a reduction in the proportion and total number of
137 CD64$^+$SiglecF$^-$ macrophages (CD45$^+$CD11c$^+$SiglecF$^-$MHCII$^+$CD11b$^+$CD64$^+$) at both day 8
138 and day 24 post-BLM (**Fig. 1d**), suggesting that IL-6 contributes to macrophage
139 recruitment to the fibrotic lung. To better characterize lung macrophages at these early
140 time points, we isolated CD64$^+$ (CD45$^+$CD11c$^+$ Siglec F$^-$MHCII$^+$CD11b$^+$CD64$^+$) and
141 alveolar (CD45$^+$CD11c$^+$Siglec F$^+$) macrophages from the lungs of BLM-treated WT mice
142 at day 5 and 14 for both transcriptional and secretome analysis. At day 5 post-BLM and
143 to lesser extent at day 14, CD64$^+$ macrophages secreted large amounts of inflammatory
144 monocyte-recruiting chemokines, CCL2, CCL3, and CCL4 (**Extended data 1a**),
145 suggesting that IL-6-dependent CD64$^+$ macrophages could contribute, in a feed forward
146 manner, to monocyte trafficking into the site of injury. Supporting this notion, deeper
147 transcriptional analysis of *ex vivo* CD64$^+$, but not alveolar, macrophages identified
148 elevated transcripts encoding a variety of inflammatory monocyte markers, cytokines,
149 and chemokines, including *Ccl8*, *Ccl12*, *Cx3cr1*, *Mmp13,* and *complement*. Of note, these
150 characteristic features have all been identified in a variety of previously reported
151 fibrogenic macrophages[29-31] (**Fig. 1e**). To determine whether IL-6 regulated the activation
152 state and recruitment of monocytes into the lung, we primed murine bone marrow-
153 derived macrophages with IL-4/IL-13 or IFNγ/LPS before exposing them to a pulse of
154 IL-6. As expected, IL-4/IL-13 up-regulated *Arg1* and *Cd206*, and, with the addition of
155 IL-6, these levels doubled, unlike IFNγ/LPS primed macrophages where *Nos2*

156 expression was unchanged with the addition of IL-6 (**Extended data 1b, 1c**). Most
157 striking was the observation that IL-6 dramatically increased both transcription and
158 secretion of CCL2 from IL-4/IL-13 primed macrophages (**Extended data 1d**), suggesting
159 that IL-6 may be a potent activating signal for fibrogenic macrophages in the lung,
160 driving the secretion of CCL2 and subsequent recruitment of monocytes.
161 Transcriptional analysis of IL-6-treated macrophages identified a suite of transcripts
162 associated with inflammatory monocytes[32] and pro-fibrotic mediators, including *Il4ra,*
163 *Vegfd, Serpina3g, Ccl2, Ccl7,* and *Ccl24* (**Extended data 1e**). To determine whether these
164 observations in murine macrophages translated to human macrophages, we primed
165 human monocyte-derived macrophages with IL-4/IL-13 and treated them with IL-6. As
166 expected, IL-6 significantly increased CCL18 transcripts and secretions, a chemokine
167 known to be prognostic for worse ILD[33,34] (**Extended data 1f**). Broader analysis of the
168 differentially expressed genes revealed that IL-6 also amplified expression of several
169 additional fibrosis-associated genes including *ENPP2*, *DHRS2*, *COL24A1*, *CXCL1*, *FZD2*,
170 and *IL17RB* (**Extended Fig 1g**). Following these mechanistic and *in vitro* observations in
171 macrophages, we reanalyzed IPF and SSc-ILD patient samples and observed that IL-6-
172 regulated macrophage genes *FCGR1A (CD64)*, *CCL2,* and *CCL18* were all increased in
173 the lung tissue of IPF (**Extended data. 2a**) or skin of SSc-ILD (**Extended data. 2b**)
174 patients. Following 24 weeks of TCZ treatment, there was a very clear and strong
175 pharmacodynamic effect on serum levels of CCL18 in the faSScinate trial (**Extended**
176 **data. 2c**), suggesting that IL-6-regulated macrophage activation in these patients may be
177 reduced. Thus, IL-6 may contribute to lung function decline in patients with ILD via an
178 inflammatory macrophage-mediated activation pathway.
179
180 **Redundant, pathogenic, and protective roles of IL-11 in the lung, liver and kidney.**
181 A closely related gp130-dependent cytokine, IL-11, has recently emerged as an
182 important contributor to lung, liver, and cardiac fibrosis[21,35-38]. We therefore profiled
183 expression of *IL11* in a variety of tissues and found it to be significantly increased in the
184 lung tissue of IPF patients (**Fig. 2a**), though not the skin of SSc patients (**Fig. 2b**).
185 Similarly, in the lung tissue of mice treated with BLM, *Il11* was elevated from as early as
186 day 2 (**Fig. 2c**). More specifically, purifying a variety of cells from the lung tissue of
187 mice, *Il11* was predominantly expressed in PDGFR^{+} fibroblasts at steady state and

188 significantly increased following BLM treatment (**Fig. 2d**). Encouraged by the *Il11*
189 expression profile in both human and murine fibrotic lung tissue, we either generated
190 or sourced recombinant murine and human IL-11 and anti-IL-11 blocking mAbs to test
191 the function and role of IL-11. We first validated that IL-11 (rmIL11, rhIL11) could
192 activate primary and fibroblast cell lines (**Extended data 3a,** ED_{50} = 15-70 ng/ml) and
193 that anti-IL-11 blocking mAbs could both bind to IL-11 (**Extended data 3b**) and block
194 rmIL-11-mediated fibroblast activation *in vitro* (**Extended data 3c**, IC_{50} = 33.4 nM).
195 Finally, we ensured that anti-IL-11 mAbs could inhibit IL-11-driven pSTAT3 *in vivo* and
196 had a favorable pharmacokinetics profile ($T_{½}$ = 15.8 days) (**Extended data 3d, 3e**). To test
197 whether IL-11 contributed to BLM-induced lung inflammation and fibrosis, we dosed
198 mice with 20 mg/kg of anti-IL-11 every week, prior to and following BLM treatment to
199 ensure complete pathway blockade. BLM treated mice lost weight and succumbed to
200 BLM exposure irrespective of IL-11 antagonism (**Fig. 2e, f**). Furthermore, elevated levels
201 of total (**Fig. 2g**) or newly synthesized (**Fig. 2h**) hydroxyproline (from day 9 – day 24),
202 was unchanged following IL-11 blockade. Similarly, increased airway infiltrates and
203 GCSF following BLM treatment were unchanged following IL-11 blockade (**Fig. 2i, j**).
204 Interestingly, we observed a small increase in circulating neutrophils following IL-11
205 inhibition (**Fig. 2k**). Finally, gene expression in lung tissue (**Fig. 2l**) and lung pathology
206 (**Fig. 2m**) confirmed that in our hands IL-11 appears to be redundant for BLM-induced
207 lung damage, inflammation, and fibrosis. To test the IL-11 pathway in a different way,
208 we sourced *Il11r*$^{-/-}$ mice and confirmed that lung fibroblasts from these mice were
209 unresponsive to rmIL-11, but responsive to rmIL-11 fused to rmIL-11 receptor (IL-11:IL-
210 11R) (**Extended data 3f, 3g**). Similar to the pharmacological approach with anti-IL-11
211 mAbs, *Il11r*$^{-/-}$ mice developed pulmonary inflammation and fibrosis similar to WT
212 (*Il11r*$^{+/+}$) mice, with comparable lung hydroxyproline content (**Fig. 2n**), fibrosis, and
213 tissue inflammation (**Fig. 2o**), and with a similar degree of airway inflammation (**Fig.
214 2p**). To more directly test whether rmIL-11 could activate lung fibroblasts, we cultured
215 WT murine lung-derived fibroblasts with rmIL-11 and assessed both inflammatory
216 cytokine secretion and ACTA2 protein expression. Although rmIL-11 could induce a
217 variety of cytokines, rmIL-11 failed to induce ACTA2 expression (**Extended data 3h, 3i**).
218 Previous studies have also implicated IL-11 in the pathogenesis of obstructive airway
219 disease, such as asthma, in both human and murine studies[39-42]. We therefore took a
220 gain- and loss-of-function approach and confirmed that rmIL-11 given to house dust

221 mite (HDM) exposed mice could enhance lymphocytic and eosinophilic airway
222 inflammation (**Fig. 2q, 2r**), with a concordant increase in BAL IL-4 and IL-5 (**Fig. 2s**). In
223 agreement with an important role for IL-11 contributing to airway inflammation, anti-
224 IL-11 treated mice had significantly reduced cellular airway infiltration and BAL
225 cytokine secretions (**Fig. 2t, 2u, 2v**). Collectively, these studies indicate that while IL-11
226 contributes to airway inflammation *in vivo* and that IL-11 can induce inflammatory
227 cytokine responses in lung fibroblasts *in vitro*, IL-11 does not appear to have fibrogenic
228 properties in the lung *in vivo* or with lung-derived fibroblasts *in vitro*. To further explore
229 the role of IL-11 in other fibrotic responses, we extended our studies into the kidney
230 using two different kidney fibrosis models, a nephrotoxic serum (NTS)-induced kidney
231 damage and fibrosis model and a unilateral ureteral obstruction (UUO) model of
232 kidney fibrosis. NTS treated *Il11r*$^{+/+}$ and *Il11r*$^{-/-}$ mice both developed similar degrees of
233 glomerular damage and fibrosis (**Extended data 4a, 4b)**. Similarly, nephropathy in WT
234 mice caused by UUO was similar between mice given control mAbs and anti-IL-11
235 mAbs, with similar levels of hydroxyproline and expression of *Col1a1*, *Tnfa,* and *Il6* in
236 the kidney (**Extended data 3c, 3d**). Finally, given the reported roles of IL-11 in the liver,
237 we tested whether IL-11 blockade could prevent the choline-deficient, L-amino acid-
238 defined, high-fat diet (CDA-HFD)-induced murine model of nonalcoholic
239 steatohepatitis. Again, anti-IL-11 mAb-treated mice had a similar increase in liver
240 weight and liver damage, with increased AST and ALT (**Extended data 4e**), as mice
241 given control mAbs. Moreover, mice fed a CDA-HFD and given rmIL-11 daily from day
242 7-11 had similar liver weight increase but significantly less liver damage with reduced
243 serum AST and ALT levels (**Extended data 4f**), indicating that IL-11 has hepato-
244 protective properties as previously indicated[43]. Thus, IL-11 contributes to airway
245 inflammation and protection from CDA-HFD-induced liver injury, but does not appear
246 to contribute to pulmonary or kidney fibrosis. This was also the conclusion from a
247 recent study by Tan and colleagues[44], who also suggested that IL-11 may not act
248 downstream of TGFβ and that IL-11 may not contribute to fibrogenesis.
249
250 **Significant and non-redundant role of OSM in pulmonary fibrosis.**
251 OSM has both positively and negatively been associated with fibrosis[19-22,25,27,28,45-47], but to
252 the best of our knowledge, the requirement for OSM and OSMR signaling in pulmonary

253 fibrosis has not been tested, genetically or pharmacologically. *OSM* was elevated
254 (though not statistically significant) in the lung tissue from IPF patients (**Fig. 3a**) and the
255 skin of SSc patients (**Fig. 3b**). Similarly, *Osm* was significantly elevated in the lung tissue
256 of BLM-treated mice from day 2 onwards (**Fig. 3c**), similar to *Il11* (**Fig. 2d**). However,
257 unlike *Il11*, *Osm* was largely restricted to $CD45^+$ cells (**Fig. 3d**). Within $CD45^+$ cells, *Osm*
258 was present in both alveolar and $CD64^+$ populations and was significantly increased in
259 $CD64^+$ macrophages following BLM treatment at day 5 and day 14 (**Fig. 3e**). To formally
260 test the requirement for OSM in BLM-induced pulmonary fibrosis we treated $Osm^{+/+}$
261 and $Osm^{-/-}$ mice with BLM. Both groups had similar weight loss (**Fig. 3f**) and survival
262 (**Fig. 3g**) post-BLM; however, $Osm^{-/-}$ mice had significantly less lung damage
263 (determined by changes in tissue volume [TV]) (**Fig. 3h**), less total and new
264 hydroxyproline deposited in the lung (**Fig. 3i, 3j**), and significantly less tissue pathology
265 (**Fig. 3k, Extended data 5a**). Interestingly, $Osm^{-/-}$ mice had a similar degree of tissue
266 inflammation as $Osm^{+/+}$ mice (**Fig. 3l**), suggesting that, in this BLM model, OSM is
267 predominantly pro-fibrotic rather than pro-inflammatory. Encouraged by these genetic
268 studies, we tested whether a pharmacological approach, using an anti-OSM blocking
269 mAb, as previously characterized[48], would afford similar benefit to WT mice exposed to
270 BLM. Similar to $Osm^{-/-}$ mice, BLM-treated WT mice given an anti-OSM blocking mAb
271 had similar weight loss and survival as WT mice given a control mAb (**Fig. 3m, 3n**), but
272 had significantly less total and new hydroxyproline deposited in the lung compared to
273 control mAb treated mice (**Fig. 3o, 3p**). Transcriptional analysis of lung tissue from anti-
274 OSM treated mice identified a variety of fibrotic pathways that were reduced following
275 OSM blockade, including significantly reduced ECM regulators (*Timp1, Mmp10, -12, -13,*
276 *-14, and -19*) (**Fig. 3q**), collagen synthesizing and regulating genes (*Col1a1, Col1a2,*
277 *Col3a1, Ereg,* and *Has2*), and, most notably, *Tnc*, which encodes the potent pro-fibrotic
278 hexameric ECM glycoprotein, Tenascin-C[49] (**Fig. 3r**). Other well-described pro-fibrotic
279 mediators, *Tgfb1, Tgfb2, Tgfb3, Il13,* and *Ctgf* experienced little change following OSM
280 blockade (**Extended data 5b**), suggesting that OSM-driven fibrosis may be independent
281 of these pro-fibrotic pathways. Finally, pathway analysis revealed the extent of the
282 benefit of OSM blockade, with several fibrotic pathways ("wound healing", "IPF
283 signaling", "pulmonary healing", "hepatic fibrosis") reduced (**Fig. 3s**).
284

285 **Combined IL-6 and OSM antagonism significantly reduces lung injury,**
286 **inflammation, and fibrosis.**
287 Collectively, data presented above identify an inflammatory IL-6-dependent $CD64^+$
288 myeloid activating pathway and an OSM-driven fibrotic pathway contributing to BLM-
289 induced lung injury, inflammation, and fibrosis. We therefore hypothesized that
290 combined blockade of IL-6 and OSM would provide both anti-inflammatory and anti-
291 fibrotic functions, respectively, to mice exposed to BLM. To test this hypothesis, we
292 treated mice with an anti-IL-6R mAb (i.e., the murine surrogate to TCZ), an anti-OSM
293 mAb (as above), or a combination of both mAbs. As expected, BLM-exposed mice
294 lost weight irrespective of mAb treatment (**Fig. 4a**), with a small proportion of mice
295 succumbing to BLM-induced disease (**Fig. 4b**). Both anti-IL-6R or anti-OSM treatment
296 reduced lung damage (determined by changes in TV) (**Fig. 4c**), but the combination of
297 anti-IL-6R and anti-OSM had the greatest impact, reducing tissue volume by
298 approximately 60% (BLM + control mAbs vs BLM + anti-IL-6R + anti-OSM, 140 ± 18.3
299 mm^3 vs 60.2 ± 9.2 mm^3). The effects of combination treatment extended to fibrotic
300 endpoints, hydroxyproline measurements, and pathology scores, with the greatest
301 reduction in these endpoints observed in mice given both anti-IL-6R + anti-OSM (**Fig.**
302 **4d-f**). Furthermore, using airway infiltrates as a surrogate for inflammation, anti-IL-6R
303 treatment successfully reduced inflammation, but the greatest effect again, especially
304 for reducing airway neutrophils, was observed in mice given both anti-IL-6R + anti-
305 OSM (**Fig. 4g**). These data indicate that IL-6 and OSM both contribute to BLM-induced
306 lung injury, inflammation, and fibrosis in a non-overlapping manner and that combined
307 antagonism of these pathways provides greater benefit than either single treatment
308 alone.
309
310 **Antagonism of IL-6R and OSM prevents myeloid cell and stromal cell activation,**
311 **respectively.**
312 To identify the cell-specific transcriptional responses of BLM treated mice and how
313 antagonism of both IL-6 and OSM pathways impact these responses, we carried out
314 single cell RNA sequencing (scRNA-seq) on lung tissue isolated from mice given
315 isotype control, anti-IL-6R, anti-OSM, or a combination of both anti-IL-6R and anti-OSM
316 mAbs on day 24 post BLM. After extensive optimization of tissue dissociation, cell

317 hashing, and the use of conventional markers, we recovered and could identify all the
318 expected cell types in the lung (**Fig. 5a, Extended Data 6a**). We assessed the proportion
319 of all major cell types in the lung in all treatment groups and observed only subtle shifts
320 in the proportion of cells with or without BLM or mAb treatment. For example, there
321 was a relative decrease in adventitial fibroblasts and increase in myofibroblasts
322 irrespective of mAb treatment (**Extended data 6b**). Similarly, there was a reduction in
323 AT2 airway epithelial cells and an increase in secretory cells post-BLM irrespective of
324 mAb treatment (**Extended data 6c**). No overt changes in the proportion of endothelial
325 cell types or lymphoid cells were observed, while a subtle increase in dendritic cells
326 (DCs) could be seen (**Extended data 6d-6f**). This scRNA-seq approach allowed us to
327 identify *Osmr* and *Il6ra* expressing cells, characterize their response to pathway
328 antagonism, and help guide subsequent mechanistic studies. Firstly, *Osmr* was
329 predominantly expressed in small airway epithelial cells (SAEC), endothelial cells
330 (ENDO), and fibroblasts (FIB) (**Fig 5b**). In contrast, *Il6ra* was predominantly expressed
331 in myeloid cells, as expected from data shown in **Figure 1**, but also in T cells (**Fig 5c**).
332
333 To identify how combination treatment provided greater benefit than either antagonist
334 alone, we first filtered differentially expressed genes (DEG) on FDR<0.05 that were
335 significantly upregulated in BLM-treated mice (BLM + isotype mAbs) relative to
336 control mice (PBS). Within these DEG, we next identified genes that were greater than
337 2-fold decreased in combination-treated mice (BLM + anti-IL-6R + anti-OSM), relative
338 to the BLM-treated mice (BLM + isotype mAbs). We show in **Fig. 5d-5i** hierarchical
339 clusters of the top 50 genes that satisfy these criteria in *Osmr*-expressing (**Fig. 5d-5g**) and
340 *Il6ra* expressing (**Fig. 5h-5i**) cell types. This approach identified cell-specific
341 transcriptional responses that were modulated by anti-IL-6R, anti-OSM, both, or
342 neither, within the genes that were modulated by combination treatment (anti-IL-6R +
343 anti-OSM). For example, within SAECs (**Fig. 5d**), BLM up-regulated the damage-
344 associated transition progenitor (DATP) marker, *AW112010*[50], in AT2 cells (**Fig. 5d***)
345 previously identified in damaged AT2 cells. Combination treatment led to >2-fold
346 reduction in *AW112010* (a filtering criteria as described above), which could also be
347 observed in SAECs in mice given either anti-IL-6R or anti-OSM, thus representing a
348 common effect of antagonizing IL-6R or OSM. In contrast, combination treatment and

349 anti-OSM alone, but not anti-IL-6R alone, prevented the SAEC expression of *Cxcl17*, a
350 chemokine upregulated in patients with IPF[50](**Fig. 5d****), highlighting a clear and
351 specific impact of antagonizing OSM, but not IL-6R. Similarly, combination treatment
352 and anti-IL-6R alone effects could be observed, including prevention of *Eno1* up-
353 regulation (**Fig. 5d*****), a serum isoenzyme biomarker associated with IPF[51],
354 highlighting the effect of antagonizing IL-6R, but not necessarily OSM. These cell type-
355 specific treatment effects could be observed within adventitial and alveolar
356 fibroblasts and endothelial cells (**Fig. 5e-g**) where *Osmr* was predominantly expressed.
357 Interestingly, anti-IL-6R treatment also appeared to prevent the upregulation of many
358 genes in fibroblasts, either reflecting the indirect effect of antagonizing IL-6R and/or a
359 potential limitation of this murine study design and/or model. Although a clear effect
360 of IL-6R antagonism could be observed across various cell types (**Fig. 5d-5i**), it was less
361 clear to see where OSM antagonism had unique cell-specific effects. Furthermore, many
362 genes in fibroblasts in combination-treated mice were indistinguishable from naïve
363 mice (**Fig 5d-I**, purple and grey treatment groups), which did not appear to be impacted
364 by either antagonist alone. These observations suggest that the transcriptional profiles
365 observed with combination treatment is greater than the sum of each part and that the
366 benefit of antagonizing both OSM and IL-6R is broad and impacts many cell types.
367

368 **OSM-driven pathogenic effects in human disease-relevant cells are OSMR-**
369 **dependent.**

370 To better understand how OSM may contribute to human fibrotic lung disease, we first
371 identified *OSMR* expression patterns in human IPF lung scRNA-seq data and found
372 *OSMR* was also predominantly expressed in endothelial cells, fibroblasts, and airway
373 epithelial cells (**Extended data 7a, 7b**), a similar pattern to that observed in mice (**Fig.**
374 **5b**). *IL6R* was also predominantly expressed in myeloid and some airway epithelial
375 cells (**Extended data 7c**). We therefore explored the impact of OSM on primary human
376 SAECs, endothelial cells, and fibroblasts *in vitro* (**Fig. 6a**). All three primary human cell
377 types responded to OSM with significant STAT3 phosphorylation, whether cells were
378 derived from healthy donors or patients with IPF (**Fig. 6b, Extended data 8a, 8b**). We
379 next carried out a comparative transcriptional analysis of these 3 cell types following 24
380 hrs. of exposure to OSM (**Fig. 6c**). Of the top 10 OSM-induced transcripts in each cell

381 type, many were commonly upregulated across all cell types (*CFI, JAK3, SOCS3, C1R,*
382 *SPP1, IL1R1, CEBPD, GSDMC, and NAMPT*), with some notable cell-specific responses
383 observed, including OSM-induced *ENNP2* (autotaxin) in SAECs, OSM-induced *IL6* in
384 endothelial cells, and OSM-induced *S1PR1* in fibroblasts, all of which have clear roles in
385 pulmonary fibrosis [11,52,53]. In addition to these transcripts, several noteworthy responses
386 were observed, including several chemokines (*CXCL12*, *CCL2*, *CXCL6*, and *CCL7*);
387 *SERPINB4* and *MMP8* in SAECs; *LRG1*, *EGR1*, and *CXCL16* in endothelial cells; and
388 *IGF1*, *CCR1*, and, in particular, *TNC* in fibroblasts[49] (**Extended data 8c**). Comparative
389 pathway analysis identified several OSM-driven inflammatory and remodeling
390 responses across cell types, including granulocyte adhesion, epithelial-mesenchymal
391 transition (EMT), macrophage activation, fibrosis, and wound healing, supporting a
392 pleiotropic and broad pathogenic role for OSM (**Extended data 8d**). Finally, to identify
393 putative OSM-induced biomarkers and pathway modulators, we compared the OSM-
394 induced responses *in vitro* in the three cell types with observed transcriptional
395 responses in the lung tissue of patients with IPF . OSM-driven *CCL2,* *CXCL1*, and
396 *CXCL6* responses in SAECs were also observed in the IPF lung samples; OSM-driven
397 *JAK3* and *TGFB3* in endothelial cells were observed in the IPF lung samples; and OSM-
398 driven *CCL2*, *DIO2*, and *ADAM12* in fibroblasts were observed in the IPF lung
399 samples (**Extended data 9a-9f**).
400
401 OSM binds to gp130 and heterodimerizes with either OSMR or LIFR for signal
402 transduction. Following the observation that antagonizing the ligand OSM, but not
403 OSMR, compromised hemoglobin and circulating platelets in patients[54,55], it was of great
404 interest to determine whether OSM-driven responses were mediated via OSMR and/or
405 LIFR. We therefore tested whether antagonizing OSMR alone was sufficient to block
406 OSM-driven responses in these 3 OSM-responsive and disease-relevant cell types.
407 Using an anti-human OSMR blocking mAb, we could almost completely inhibit OSM-
408 induced pSTAT3 in SAECs and fibroblasts (**Fig. 6d**), whether derived from healthy or
409 IPF donors (**Extended data 10a**), but could only inhibit OSM-induced pSTAT3 in
410 endothelial cells by approximately 50% (**Fig. 6d, Extended data 10b**). The addition of
411 anti-LIFR to anti-OSMR treated endothelial cells resulted in complete inhibition of
412 OSM-induced pSTAT3, supporting the notion that OSM uses both OSMR and LIFR for
413 signaling in endothelial cells (**Fig. 6e**). Collectively these data indicate that OSMR

414 antagonism alone is sufficient to almost completely mitigate OSM-driven pSTAT3 in
415 fibroblasts and epithelial cells, but only partially inhibit OSM-induced pSTAT3 in
416 endothelial cells.
417
418 It has previously been reported that *in vitro* OSM can induce skin endothelial cell
419 damage[56]. We therefore moved beyond proximal activation and signaling (pSTAT3) and
420 assessed whether OSM also caused lung endothelial cell damage and whether this was
421 dependent on OSMR or LIFR. Indeed, OSM induced endothelial cell disruption and
422 permeability, compromising barrier integrity, which could be completely prevented
423 with anti-OSMR antagonism (**Fig. 6f**). Anti-LIFR mAb treatment had little to no impact
424 on OSM-induced permeability. Similarly, OSM-induced IL-6 and CCL2/MCP1
425 secretion from lung endothelial cells was largely dependent upon OSMR rather than
426 LIFR (**Extended data 10c**). Thus, despite OSM-induced pSTAT3 being only partially
427 mediated by OSMR, endothelial cell permeability and inflammatory cytokine
428 production was predominantly mediated by OSMR. We carried out similar studies with
429 primary lung SAECs grown in 3D organoids at an air liquid interface (ALI). Similar to
430 endothelial cells, OSM could also disrupt SAEC integrity with a significant increase in
431 permeability (**Fig. 6g**). OSM-driven SAEC permeability was also dependent upon
432 OSMR and not LIFR, in line with pSTAT3 data (**Fig. 6d**). Taken together these data
433 indicate that OSM can disrupt both epithelial and endothelial cell integrity, a potential
434 pathogenic axis in ILD, and that this process is dependent upon OSMR signaling.
435
436 Most strikingly, and supporting previous studies[18], OSM directly induced collagen
437 (COL1) secretion from primary human fibroblasts. This process was also OSMR-
438 dependent (**Fig. 6h**), giving some of the clearest direct mechanistic evidence for a role of
439 OSM in human fibrotic diseases. As mentioned earlier, the ECM glycoprotein, tenascin-
440 C (TNC), has pro-fibrotic properties[49]. In addition to OSM-induced expression of *TNC*
441 in fibroblasts (**Extended data 8c**) and the upregulation of *TNC* in IPF lung tissue
442 (**Extended data 9c)**, we also observed that OSM induced TNC protein secretion from
443 fibroblasts, which was also completely dependent on OSMR (**Fig 6i**). *TNC* expression
444 was significantly increased in skin biopsies from patients with SSc (**Extended data 10d),**
445 and TNC protein was clearly detected in IPF lung tissue (**Extended data 10e**).

446 Furthermore, *TNC* expression in IPF lung tissue correlated with *OSMR* expression
447 (**Extended data 10f**). Of note, TNC was significantly increased in mice given BLM, with
448 anti-OSM preventing this upregulation (**Fig. 3r**), suggesting that OSM contributes
449 significantly to TNC levels *in vitro* and *in vivo*. These data provide a second OSM-driven
450 mechanism of fibrogenesis.
451
452 Similar to OSM, TGFβ1 has been reported to co-opt STAT3 to drive fibrotic responses[57],
453 induce TNC[58,] and has clear roles in a variety of fibrotic diseases[59]. It has also been
454 reported that OSM can inhibit TGFβ1 signaling[45,60,61]. We therefore felt it was important
455 to understand the relationship between these two pro-fibrotic mediators and determine
456 whether TGFβ1 impacted OSM-induced TNC and COL1 secretion from fibroblasts. In
457 contrast to previous reports[45,60,61], we found that TGFβ1 further increased TNC and
458 COL1 from primary lung fibroblasts when given with OSM (**Fig. 6j, Extended data 10g**)
459 a process that was neither OSMR or STAT3-dependent (**Fig. 6k**). These data indicate
460 that OSM- and TGFβ1-mediated fibroblast activation is independent and non-
461 overlapping, in agreement with other studies[18].
462
463 Finally, soluble OSMR (sOSMR) can be readily detected in circulating plasma of healthy
464 subjects in the range of 80 ng/ml, and is significantly elevated, up to 450 ng/ml, in
465 patients with SSc[62]. We therefore tested whether exogenous sOSMR functioned as a
466 decoy receptor for OSM-mediated fibroblast activation and more importantly whether
467 sOSMR interfered with anti-OSMR mediated blockade of OSM. As previously
468 reported[63], sOSMR alone (up to 10μg/ml) did not function as a decoy receptor and did
469 not block OSM-induced pSTAT3 in primary human fibroblasts (**Fig. 6l**). Introduction of
470 sOSMR only started to impact anti-OSMR mediated blockade of OSM at 25μg/ml and
471 above, approximately 50 times what has been observed in patients with SSc[62].
472
473 Using three disease-relevant cell types in monocultures, we demonstrate a clear role for
474 OSMR-dependent OSM activity that drives multiple disease-relevant activation,
475 transcriptional, and physiological responses (**Fig. 6a-m**). To determine whether OSMR
476 is also required for OSM-driven responses in multi-cellular human lung explants, we

477 stimulated precision cut lung slices (PCLS) with OSM and treated these cultures with
478 anti-OSMR or anti-LIFR blocking mAbs. In agreement with the primary human
479 monoculture systems, OSM-driven chemokine production (CCL3 and CCL4) from
480 PCLS were dependent upon OSMR and not LIFR (**Fig. 6n**), supporting the therapeutic
481 targeting of OSMR to prevent OSM activity in human lung diseases. Collectively these
482 studies provide biological rationale and mechanistic data to support the therapeutic
483 development of an OSMR antagonist to treat fibrotic lung diseases. The proposed
484 benefit of OSMR antagonism may be further enhanced with the combined treatment
485 with IL-6R antagonists.

Discussion

ILDs have a devastating prognosis with life expectancy less than half a decade following diagnosis for many IPF patients. Stalling progressive fibrosis and preserving lung function are key treatment goals in patients with ILD[64]. In this study, we have characterized an IL-6-dependent inflammatory monocyte/myeloid circuit that contributes to experimental lung inflammation and pathology and correlates with several clinical observations in patients with ILD. At the heart of this axis, we observed an IL-6-driven chemokine response from myeloid cells. *In vitro*, IL-6 induced CCL18 transcription and secretion from human cells, a response which mapped to an IL-6-dependent CCL18 response in patients with ILD treated with tocilizumab. This IL-6-driven pathway has previously been implicated in, and is prognostic for, worse disease[33,34]. Similarly, in murine cells, IL-6-induced CCL2, CCL3, and CCL4 (a murine CCL18 orthologue does not exist), in agreement with previous studies showing that adenovirus-driven over-expression of IL-6 led to CCL2 secretion and lung inflammation[23]. This IL-6-driven feed-forward chemokine loop was most evident in *Il6r*$^{-/-}$ mice treated with BLM, leading to a stunted CD64^{+} inflammatory monocyte response and reduced downstream pathology. In addition to IL-6-driven chemokine responses in myeloid cells, transcriptional analysis revealed a variety of fibrosis-associated genes in both human and murine cells (*Aqp3*, *Muc1*, *Enpp2*, and *Cd64*), in line with recent observations describing a pro-fibrotic state of macrophages [29-31]. These broad IL-6 driven inflammatory and pro-fibrotic responses may be an important aspect of the clinical benefit with TCZ, as therapeutically targeting a single IL-6-driven chemokine, such as CCL2, has previously been unsuccessful in ILD [65]. Although there is a lot of interest in therapeutically targeting myeloid cells, our mechanistic hypothesis suggests that dampening inflammatory monocyte activation and numbers may reduce lung function decline, as observed with TCZ, but may not necessarily impact established and progressive fibrosis.

To this end, we focused our efforts on identifying non-redundant and non-overlapping pro-fibrotic factors that could be targeted and combined with standard of care or anti-inflammatories, including IL-6R antagonists, to prevent fibrosis. Exploring the role of other gp130-dependent cytokines, we were excited to see the emerging role of IL-11 in

518 driving fibrosis in a variety of fibrotic tissues including the liver[66,67], lung[36,37] and heart[38].
519 We also observed upregulated IL-11 in IPF and SSc tissue and in BLM-treated mice.
520 However, blocking the ligand with anti-IL-11 mAbs or genetically deleting the receptor
521 did not impact inflammatory or fibrosis-related endpoints in mice treated with BLM in
522 our hands. Similarly, in two kidney fibrosis models and a liver injury model we did not
523 observe any impact of IL-11 blockade on fibrosis-related readouts, but instead observed
524 a small hepato-protective effect of IL-11. Anti-IL-11 blocking mAbs could sufficiently
525 block IL-11 activity *in vitro* and *in vivo*, had very good PK properties, and could
526 effectively reduce HDM-induced airway inflammation, similar to previous reports[14,40-42],
527 so we were not overly concerned with our reagents. Although studies were carried out
528 over multiple geographic sites using littermate mice or control mAbs[68], there is a chance
529 that differences in microbiota may impact the sensitivity of mice to IL-11, contributing
530 to the discrepancies with other reports; however, we feel that this is unlikely. Finally,
531 using primary human fibroblasts *in vitro* we found no evidence for a pro-fibrotic role for
532 IL-11, demanding a refocus of our efforts onto other putative pro-fibrotic factors.
533
534 OSM has been very well studied in a variety of contexts, including pulmonary fibrosis[19-
535 22,25,27,28,45-47], but whether OSM is necessary for pulmonary fibrosis has not been reported.
536 As we demonstrate here, using anti-OSM blocking mAbs or *Osm*$^{-/-}$ mice, OSM has a
537 clear role in contributing to BLM-induced lung damage and fibrosis, and this role
538 appears to be non-redundant with the IL-6 pathway. As we previously reported[48],
539 microbial triggers are potent inducers of OSM from myeloid cells, and both microbial
540 dysbiosis and myeloid cell activation have both been observed and experimentally
541 confirmed as important contributors to pulmonary fibrosis in pre-clinical models[29-31,69,70].
542 Whether microbial triggers contribute to myeloid cell secretion of OSM in ILDs is
543 unclear, but may represent a targetable upstream trigger.
544
545 The non-overlapping function of OSM with IL-6 was evident in combination studies
546 where mice treated with both anti-OSM and anti-IL-6R mAbs received greater benefit
547 than either anti-OSM or anti-IL-6R treatment alone. These non-overlapping functions of
548 IL-6 and OSM have previously been implicated, with OSM-driven bronchial lymphoid
549 structures developing independent of IL-6[71], and with over-expression of OSM driving
550 connective tissue fibrosis independent of IL-6[24]. To identify the cellular responses and

551 putative mechanisms of IL-6 and OSM, we initially followed the expression of the
552 receptors for IL-6 and OSM, which pointed us towards hematopoietic and non-
553 hematopoietic compartments, respectively. These observations further separated these
554 two cytokines and supported our IL-6 mechanistic studies with myeloid cells (**Fig. 1**),
555 while also directing our OSM mechanistic studies on parenchymal and stromal cells *in*
556 *vitro* and *in vivo*. Transcriptional analysis of total lung tissue and single cell analysis of
557 OSMR-expressing cells in lung tissue from mice treated with BLM and anti-OSM
558 highlighted a broad, but somewhat subtle single cell impact of OSM (**Fig. 3 and Fig. 5**).
559 Tissue level analysis revealed a broad dampening of fibrotic pathways following OSM
560 antagonism, including reduced *Mmps*, *Timp1*, a variety of collagen synthesizing genes,
561 and *Tnc*. Single cell RNAseq analysis of lung tissue from anti-OSM treated mice focused
562 on identifying the unique contribution of OSM antagonism in OSMR-expressing cells,
563 relative to mice receiving both anti-IL-6R and anti-OSM. Clear transcriptional impacts
564 in SAECs and fibroblasts were observed, and to a lesser extent in endothelial cells,
565 while hematopoietic cells were largely unaffected (**Fig. 5**), again supporting a non-
566 overlapping mechanism of IL-6 and OSM. Mice receiving both anti-OSM and anti-IL-6R
567 treatment led to much more profound protection, both pathologically (**Fig. 4**) and
568 transcriptionally in OSMR-expressing cells (**Fig. 5**), with many genes and pathways
569 indistinguishable from non-BLM control mice.
570
571 The clearest and potentially most translatable mechanistic observations came from
572 primary human cell studies, revealing the pleiotropic impact of dysregulated OSM in
573 disease-relevant cells. Damage to airway epithelial and endothelial cells and subsequent
574 activation of fibroblasts has been a long-held hypothesis contributing to the etiology
575 and/or progression of pulmonary fibrosis[72-74]. Here we observed that OSM can
576 contribute to all three of these processes *in vitro*, from disrupting epithelial and
577 endothelial cell integrity and inducing inflammatory cytokine production, to promoting
578 collagen and TNC secretion from fibroblasts. Comparative transcriptional analysis in all
579 three cell types revealed several common pro-fibrotic transcripts upregulated by OSM
580 (**Fig. 6**), including osteopontin (*SPP1*), which is both fibrogenic and a biomarker of
581 progressive fibrosis[75-77] and NAMPT, which regulates intracellular NAD and can be
582 excreted (eNAMPT) to function as a DAMP and contribute to pulmonary fibrosis[78]. One
583 of the most interesting OSM-driven responses was TNC, the pro-fibrotic ECM

584 glycoprotein[49,58,79]. It has previously been reported that mice deficient in *Tnc* are
585 protected from BLM-induced lung and skin fibrosis and resolve fibrotic scars quicker.
586 In these studies, TNC appears to be regulated by and required for TGFβ-mediated
587 fibrosis[49,58]. In our *in vivo* studies, *Tnc* was up-regulated in BLM-treated mice and
588 significantly down-regulated following anti-OSM (**Fig. 3**), suggesting that OSM, in
589 addition to TGFβ, is an important regulator of *Tnc*. Using primary human fibroblasts,
590 TNC was secreted following OSM exposure, in an OSMR-dependent manner (**Fig. 6**).
591 When OSM was combined with TGFβ we observed even greater TNC secretion, an
592 OSM-driven response that was again dependent upon OSMR and STAT3. In contrast,
593 TGFβ induced TNC was independent of OSMR or STAT3, challenging the notion that
594 OSM inhibits TGFβ and that TGFβ-driven responses are dependent upon STAT3[57,60,61].
595
596 In conclusion, this study has characterized an IL-6-driven mechanistic pathway and
597 identified an important and non-redundant role for OSM in driving tissue damage and
598 fibrosis. From *in vitro* studies, it is clear that the majority of pathogenic OSM-induced
599 responses are dependent on OSMR, rather than LIFR, focusing our attention on the
600 development of OSMR, rather than LIFR, antagonists, mitigating the deleterious impact
601 of antagonizing OSM[54,55]. We hypothesize that antagonizing both OSMR and IL6R
602 pathways will stall progressive fibrosis and preserve lung function by preventing small
603 airway epithelial and endothelial cell damage, fibroblast activation and collagen
604 deposition and myeloid cell activation.

605 # Methods

606 **Primary human cell cultures**

607 Normal- or IPF-derived fibroblasts (FIB) were purchased from Lonza (#CC-2512, #CC-
608 7231, respectively). Human pulmonary alveolar epithelial cells (SAEC) were purchased
609 from Cell Biologics (#H-6053). Lung microvascular endothelial (ENDO) cells were
610 purchased from Lonza (#CC-2527) and Promocell (#C-12281). All cells were thawed
611 and expanded according to each manufacturer's recommendation and used before or at
612 passage 5.

613

614 **Human precision cut lung slices (PCLS)**

615 Healthy whole lungs were received from the National Disease Research Interchange.
616 The smallest lobe was cut free, exposing its main bronchiole, and inflated with 2%
617 (wt/vol) low-melting-point agarose solution. Once the agarose had solidified, the lobe
618 was sectioned. Cores of 8 mm in diameter were made in which a small airway was
619 visible. The cores were placed in a Krumdieck tissue slicer (Alabama Research &
620 Development Model no. MD4000), and the speed was set to produce slices at
621 approximately 1 per 30 seconds. PCLSs (thickness, 250 μm) were transferred in
622 sequence to wells containing Ham's F-12 medium to identify contiguous airway
623 segments. Suitable airways on slices were selected on the basis of the following criteria:
624 presence of a full smooth muscle wall (cut perpendicular to direction of airway),
625 presence of beating cilia and internal folding of epithelium to eliminate blood vessels,
626 and presence of unshared muscle walls at airway branch points to eliminate possible
627 counteracting contractile forces. Slices were then incubated at 37°C on a rotating
628 platform in a humidified air/CO_2 (95%/5%) incubator. PCLS were cultured in complete
629 DMEM and stimulated with OSM (25ng/ml) with or without anti-human OSMR or
630 anti-human LIFR.

631

632 **Reagents and antibodies**

633 Recombinant Oncostatin M (OSM) and TGF-®1 was purchased from R&D systems. All
634 cytokines in the Cytomix (TNF-α, IL-1β, IL-6 and IFN-γ) were purchased from
635 Peprotech, reconstituted in single tube aliquots and stored at -80°C until use.
636 Neutralizing anti-OSMR and anti-LIFR IgG1 antibodies were produced internally at

637 Genentech. rmIL-11 and rhIL-11 were purchased from R&D and generated internally at
638 Genentech. Anti-IL-11 mAb was used at 20mg/kg *in vivo* (MAB418, R&D or internal
639 generated anti-mouse IL-11 mAb. sOSMR was generated internally at Genentech. SD36,
640 the STAT3 degrader, as previously reported[77], was purchased from MedChem Express.
641

642 **Isolation and culture of BMDMs**

643 Femurs and tibias were harvested from mice, flushed to obtain marrow cells and passed
644 through a 70 ⌈M filter. Cells were grown on non-tissue culture treated plates in media
645 (high glucose DMEM, 10%FBS, 10 U/ml penicillin/streptomycin, 2 mM L-Glutamine, 1
646 mM sodium pyruvate) containing 50 ng/ml recombinant murine M-CSF (50ng/ml,
647 Peprotech). On day 6 macrophages were harvested, counted and re-plated for
648 experimentation. Polarization of macrophages was carried out by addition of IL-4 (20
649 ng/ml, R&D Systems), IL-13 (20 ng/ml, R&D Systems), and IL-6 (20 ng/ml, R&D
650 Systems) for 24 hours.
651

652 **Isolation and culture of human monocyte derived macrophages**

653 Monocytes were isolated from buffy coats using RosetteSep human monocyte
654 enrichment cocktail kit (Stem Cell, Cat No, 15028) according to manufactures
655 instructions. Cells were grown on non-tissue culture treated plates in media (RPMI,
656 10%FBS, 10 U/ml penicillin/streptomycin, 2 mM L-Glutamine) containing 50 ng/ml
657 recombinant murine M-CSF (50ng/ml, Peprotech). On day 10 macrophages were
658 harvested, counted and re-plated for experimentation. Polarization of macrophages was
659 carried out using IL-4 (20 ng/ml, R&D Systems), IL-13 (20 ng/ml, R&D Systems) and IL-
660 6 (20 ng/ml, R&D Systems).
661

662 **Mice**

663 All experiments were conducted in accordance with protocols approved by the
664 Institutional Animal Care and Use Committee at Genentech (IACUC) and at Chugai,
665 Singapore. WT Male (C57BL/6J), 15-20 weeks of age were purchased from the Jackson
666 Laboratory or bred internally. The mice were kept on a 12h light-dark cycle with free
667 access to food and water and were used in accordance with the *Guide for the Care and*
668 *Use of Laboratory Animals.* IL-6 receptor knockout (*Il6r*$^{-/-}$) mice were generated as

669 previously described[80]. Briefly, mice with a conditional allele (*Il6r*$^{f/fl}$)[79] were interbred
670 with Rosa26.Cre (Taconic) and maintained on C57BL/6 strain. C57BL/6 *Osm*$^{-/-}$ mice
671 were purchased from MMRRC (C57BL/6N-*A*^{tm1Brd} *Osm*$^{tm1b(KOMP)Wtsi}$/JMmucd; MMRRC
672 Stock number 048921-UCD).
673
674 **Airway disease models.**
675 **Mouse model of bleomycin (BLM)-induced lung injury, inflammation and fibrosis**.
676 Mice were randomized based on pre-study weights to minimize variance between
677 experimental and control groups. For disease induction, mice were lightly anesthetized
678 with isoflurane in an induction chamber. Once anesthetized, the animals were removed
679 from the chamber, manually restrained, the mouth of the animal was opened, the
680 tongue set aside and a 200uL microtip placed on the trachea. A solution of bleomycin
681 (0.75 U kg^{-1} (DNC# 0703-3155-01; TEVA) prepared in PBS or saline was then instilled in
682 the trachea. After delivery, animals were monitored continuously until fully awake and
683 ambulatory. Bleomycin or saline control was administered equally in subtherapeutic
684 doses over 3 separate days (M, W, F). Unless otherwise stated, mice were analyzed at
685 day 24 after the 1st bleomycin administration. **House Dust mite (HDM) model.** For
686 house dust mite (HDM)-induced airway inflammation, mice were anesthetized with an
687 i.p. injection of Ketamine 40mg/kg with Dexmedetomidine 1mg/kg. Once
688 anesthetized, mice were treated with HDM (Greer, 10μg in 25μl) by the intratracheal
689 route. Mice were treated with HDM on day 0, 2, 4, 14, 16, 27 and 29 and analyzed on
690 day 30. In some experiments mice were treated with rmIL-11 (10μg in 25μl) on day 27
691 and 29 and analyzed on day 30. In some experiments mice were treated with anti-
692 mouse IL-11 (500ug/mouse) on day 16, 27 and 29 and analyzed on day 30. **Broncho-**
693 **alveolar lavage (BAL)** was collected in two sequential recoveries. Firstly, 500μl of ice-
694 cold PBS was used to lavage the airspaces for cellular and analyte analysis. A second
695 lavage of 2 x 500μl was used for additional cellular recovery. Total BAL cells and
696 differential cell counts were determined from two BAL washes. Firstly, with 500μl of
697 sterile cold PBS for analyte analysis and cellular recovery and then with 1ml of sterile
698 cold PBS for cellular recovery.
699
700 **Lung cell isolation for FACS and tissue bulk RNA sequencing**

701 Lungs were harvested, disrupted using Gentle MACS (Miltenyi) then incubated in
702 Liberase TM, 100 ug/ml (Roche) and DNase I, 0.33 mg/ml (Roche) at 37°C for 30 minutes
703 with gentle agitation before a final disruption using Gentle MACS (Miltenyi). The tissue
704 was then passed through a 70-µm nylon filter to obtain a single cell suspension. Cells
705 were treated with Ammonium-Chloride-Potassium (ACK) lysis buffer to remove
706 erythrocytes then cells were processed for RNA analysis and FACS staining. **FACS**
707 **staining and sorting.** Single cell suspensions were first treated with mouse FcR blocking
708 reagent (Miltenyi, 130-092-575) for 10 minutes then stained for 40 minutes with
709 combinations of antibodies to CD45 (clone 30-F11, BD Pharmingen), CD11c (clone N418,
710 Biolegend), Siglec F (clone E50-2440, BD Pharmingen), MHCII (clone M5/114.15.2,
711 eBioscience), CD11b (clone M1/70, Biolegend), CD64 (clone X54-5/7.1, Biolegend) and
712 F4/80 (clone BM8, Biolegend), CD206 (clone MMR, Biolegend). Dead cells were excluded
713 using the live/dead fixable aqua dead cell stain kit (Life Technologies, L34957). **FACS**
714 **sorting.** Myeloid cells were enriched from single cell suspensions of mouse lung tissue
715 using CD11c microbeads (Miltenyi, 130-097-059) as per manufacturer's instructions and
716 stained for FACS markers as described in each experiment.
717
718 **Lung histology staining and analysis**
719 Mouse lungs were inflated with 1ml of 10% paraformaldehyde/PBS solution,
720 embedded as a whole in paraffin and processed to 2 (5-⌠m thick) slides per animal, one
721 series stained with Masson's Trichrome and the other with H&E. The extent of
722 pulmonary fibrosis was scored on the Masson's Trichrome-stained slides according to
723 the following criteria: (A) Interstitial fibrosis pattern—number of foci: 0, none detected;
724 1, ≤10; 2, ≤15; 3, >15/all sections, but distinct; 4, multifocally coalescent or locally
725 extensive; 5, diffuse. (B) Interstitial fibrosis—size of foci: 0, none detected; 1, largest
726 focus ≤area of ~2 alveolar spaces; 2, largest focus ≤ area of ~4 alveolar spaces; 3,
727 coalescent (>4 patent alveolar spaces); 4, locally extensive (60–90% of an entire lobe); 5,
728 diffuse (>90% of an entire lobe). (C) Total scores: number of foci × size of foci. The
729 extent of lung inflammation was scored on the H&E-stained slides according to the
730 following criteria: 0, normal lung (no inflammatory infiltrate); 1, minimal disease
731 (infrequent sparsely scattered inflammatory cells); 2, mild (light perivenous/subpleural
732 involvement); 3, moderate (many foci of small mononuclear cells extending over 3-5

733 alveoli); and 4, severe (generalized accumulations of small mononuclear cells involving
734 >5 alveolar spaces).
735
736 **Hydroxyproline measurement**
737 Total hydroxyproline was analyzed as previously described[81] and mass spectrometry
738 analysis was performed by Metabolic Solutions. Deuterated water labeling was used to
739 assess new collagen synthesis. In brief, mice were injected with deuterated water (DLM-
740 4-99.8-1000; Cambridge Isotope Laboratories) intraperitoneally two weeks prior to the
741 end of the study at 35 mL/kg in 2 divided doses 4 h apart. Afterward, 8% deuterated
742 water in drinking water was provided ad libitum in water bottle until the end of the
743 study. Mass spectrometry and analysis were performed by Metabolic Solutions.
744
745 **Kidney and Liver Fibrosis models**
746 **Unilateral Ureteral Obstruction (UUO) model.** C57BL/6NTac male mice of 6 weeks
747 were purchased from Invivos Pte Ltd (Singapore) and were acclimated for 1 weeks
748 before the start of study. Mice were randomized to the sham group (n=4), UUO group
749 (n=8), and anti-IL11 antibody (Clone 5A6) treatment group (n=8). UUO surgery was
750 operated under isoflurane anesthetized condition as previously described[82]. All
751 monoclonal antibodies were administered at 50 mg/kg by intravenous injection one
752 day before the surgical operation. Mice were ethically sacrificed 7 days after UUO
753 establishment. The hydroxyproline contents in kidney was measured using
754 hydroxyproline assay kit (BioVision). Total RNA was extracted using RNeasy Mini Kit
755 (Qiagen), and cDNA was synthesized using a Transcriptor Universal cDNA Master
756 (Roche Diagnostics). Quantitative PCR was performed with a TaqMan Gene Expression
757 Assay (Thermo Fisher Scientific) and expression levels and mouse mitochondrial
758 ribosomal protein L19 (MRPL19) was used as the endogenous reference for each
759 sample. Relative mRNA expression values were calculated using double delta Ct
760 analysis. **Choline-deficient, L-amino acid-defined, high-fat diet (CDA-HFD) model**
761 C57BL/6NTac male mice of 6 weeks of age were purchased from Invivos Pte Ltd
762 (Singapore) and were acclimated for 1 week before the start of treatments. Choline-
763 deficient, L-amino acid-defined, high-fat diet (CDAHFD; #A06071302), was purchased
764 from Research Diets (New Brunswick, NJ, USA) and fed to induce disease. 5P75 was fed

765 as a normal diet. In some experiments mice were treated with anti-mouse IL-11
766 antibody (15 and 50mg/kg) on day 0 and 7 and analyzed on day 14. In some
767 experiments mice were treated with rmIL-11 (R&D systems, 25 and 100ug/kg) from day
768 7 to 11 and analyzed on day 11. Livers were harvested and weighted. Plasma AST and
769 ALT was measured by ALT or AST Activity Colorimetric/Fluorometric Assay Kit (Bio
770 Vision). **Murine Nephrotoxic Nephritis model.** For nephrotoxic serum (NTS)-induced
771 kidney fibrosis, mice were injected i.v. with 5 μl/g saline (control) or sheep anti-rat
772 glomeruli serum (NTS; Probetex) on day 0 and monitored to 42 days post injection
773 when they were euthanized and one kidney was submitted for histologic evaluation.
774 Glomerulonephritis and fibrosis were evaluated according to the following metrics.
775 Glomerular Scoring Matrix: (0) Within normal limits. (1) Mild, segmental mesangial
776 expansion with or without increased cellularity. (2) Moderate, segmental mesangial
777 expansion frequently associated with increased cellularity. (3) Global
778 membranoproliferative glomerulonephritis. (4) Glomerulosclerosis. Twenty glomeruli
779 were scored per mouse. Fibrosis Scoring Matrix: (0) No appreciable increase in peri-
780 glomerular fibrosis. (1) 5 or fewer individual tubules or glomeruli with surrounding
781 fibrosis. (2) >5 individual tubules or glomeruli with fibrosis and/or 5 of few foci of
782 interdigitating interstitial fibrosis. (3) >5 interdigitating regions of interstitial fibrosis or
783 1-2 regions of expansive fibrosis. (4) 3-5 foci of regionally expansive fibrosis. (5) >5 of
784 regionally expansive fibrosis.
785
786 **Scar-in-a-jar assay.**
787 Mature extracellular collagen and tenascin-C fiber deposition was assayed as previously
788 described[83]. Briefly, Normal- or IPF-derived human lung fibroblasts were seeded at
789 10,000 cells/well in complete FGM-2 media overnight. Following 2 hours pre-treatment
790 with anti-OSMR IgG1 antibodies, isotype controls or the STAT3 degrader (SD-36), cells
791 were incubated with OSM (10ng/mL) and/or TGF-®1 (1ng/mL) in Ficoll media for 72
792 hours. At harvest, cells were fixed with 4% paraformaldehyde supplemented with 4%
793 sucrose, blocked with PBS-2% BSA and stained overnight with mouse anti-collagen 1
794 (#C2456; Sigma) or anti-tenascin-C antibodies (#ab3970; Abcam). The following day,
795 cells were stained with AlexaFluor 488-conjugated anti-mouse antibodies (#A-11001;
796 Life Technologies) and Hoechst 33342 (#H3570; Fisher Scientific) and data was acquired

797 on the high-content imaging platform (CellInsight CX7; Thermo Fisher). All
798 intermediate washes were performed with PBS-0.05% Tween 20.
799
800 **Cell permeability (XPerT) assay**
801 Lung microvascular endothelial cells were seeded on gelatin-biotin-coated black plates
802 at 30,000 cells per well and left in EGM-2MV media (#CC-3202; Lonza) to form a
803 homogeneous monolayer for 72 hours. Where indicated, cells were pre-treated with
804 anti-OSMR and/or anti-LIFR antibodies for 2 hours. Insult was induced by addition of
805 OSM or Cytomix [1X = TNF-α, 0.25ng/mL; IL-1β, 0.2ng/mL; IL-6, 0.25ng/mL; IFN-γ,
806 1ng/mL], or PBS for controls, and plates were incubated for 20-24h. At harvest, plates
807 were stained with Neutravidin-Dylight 488 (#22832; Thermo Scientific), washed and
808 relative fluorescence intensity was acquired on a Synergy HT (BioTek) microplate
809 reader. SAEC were seeded at 12,500 cells/well in Small Airway Epithelial Cell Growth
810 Medium (SAGM) (#CC-3118; Lonza) into 96-well transwell inserts. The next day, both
811 the apical and basolateral media was exchanged with SAGM media supplemented with
812 100 nM Dexamethasone (#D4902; Sigma), 5 ng/mL Human FGF-7 (#PHG0094; Thermo
813 Fisher Scientific, 50 uM 8-Br-cAMP (#B7880; Sigma) and 25 uM IBMX (#I7018; Sigma).
814 Two days later, the cells were airlifted by removing the media from the apical chamber
815 of the transwell and the media in the basolateral chamber was exchanged with
816 DMEM:F12 containing 2 mM Glutamax, 100U/mL Penicillin, 100 ug/mL Streptomycin,
817 and 250 ng/mL amphotericin B. The media in the basolateral chamber was change
818 every 2-3 days until the end of the airlifting period (11-13 days). When indicated,
819 airlifted SAEC were pre-treated with anti-OSMR and/or anti-LIFR antibodies for 2
820 hours. Insult was induced by addition of 12.5-25 ng/mL OSM or Cytomix [1.5-5X=
821 TNF-α at 0.3-0.6ng/mL; IL-1β at 0.3-0.5ng/mL; IL-6 at 0.3-0.5ng/mL; IFN-γ at 1.3-1.9
822 ng/mL], or media for controls. After 20-24h incubation, the transwells were moved to
823 receiver plates containing 200 uL of Transport Buffer (HBSS, 10 mM HEPES, pH 7.4) in
824 the basolateral chamber. The apical volume was aspirated and replaced with 100 uM
825 Lucifer Yellow (#L453; Thermo Fisher Scientific) in Transport Buffer and the
826 quantitation of Lucifer Yellow in the basolateral chamber was measured (Ex428, Em536)
827 after 3 hours of translocation time. The remaining Lucifer Yellow solution in the apical

828 chamber was then aspirated, replaced with Cell Titer Glo Reagent (#G7570; Promega)
829 and luminescence was recorded after 10 min.
830
831 **Luminex Assay**
832 Human and murine chemokine and cytokine concentrations were assayed by Luminex
833 technology using Bio-Plex Pro (Bio-Rad Laboratories) according to manufacturer's
834 instructions. Fluorescence Intensities (FI) from the labelled beads were read using
835 FlexMaps instrument (Luminex Corp). FI from diluted standards were used to construct
836 standard curves using Bio-Plex Manager software (Bio-Rad Laboratories) using either 4-
837 pl or 5-pl regression type. Data is presented as average of duplicate measurements.
838
839 **Surface plasmon resonance**
840 The binding kinetics of anti-IL11 antibody MAB418 was measured using surface
841 plasmon resonance (SPR) on a Biacore 8k+ instrument (Cytiva). MAB418 was directly
842 immobilized on a CM5 Series S sensorchip using amine coupling. Antibody binding
843 was measured to mouse IL11 using a concentration series starting with 300 nM with one
844 to three dilutions. Sensorgrams for binding of cytokine were recorded using an
845 injection time of 2 minutes with a flow rate of 30 ul/min, at a temperature of 25˚C, and
846 with a running buffer of 10mM HEPES, pH 7.4, 150 mM NaCl, 3 mM EDTA, and 0.005%
847 Tween 20. After injection, disassociation of the cytokine from the antibody was
848 monitored, and the surface was regenerated between binding cycles with 10 mM
849 Glycine HCl pH 1.7. After subtraction of a blank which contained running buffer only,
850 sensorgrams observed for cytokine binding to MAB418 were analyzed using a 1:1
851 Langmuir binding model with software supplied by the manufacturer.
852
853 **MSD Assay**
854 Murine and Human phospho-STAT3 (Tyr705) (#K150SVD-4; Meso Scale Discovery)
855 was measured in total cell lysates per manufacturer's recommendation.
856
857 **Immunohistochemistry (IHC)**
858 Cells were fixed with 4% formaldehyde in PBS for 15 minutes, washed 3 times for 5
859 minutes in PBS, then blocked and permeabilized with a 1× PBS/5% normal goat

860 serum/0.3% Triton X-100 solution for 1 hour at room temperature. A mouse
861 monoclonal antibody to α-Smooth Muscle Actin (MAB1420, R&D Systems) was diluted
862 to 15ug/ml in a 1× PBS/1% BSA/0.3% Triton X-100 solution and incubated overnight at
863 4°C. Slides were washed 3 times with PBS and incubated in secondary antibody at a
864 concentration of 1ug/ml in PBS (A-11001, Thermo Fisher Scientific) for 1 hour at room
865 temperature. Samples were washed 2 times for 5 minutes with PBS, and mounted with
866 DAPI-containing ProLong Gold Antifade Mountant (Thermo Fisher Scientific). Images
867 were taken on a Zeiss Axio Imager M2 microscope. A panel of 174 rabbit-derived
868 monoclonal antibodies raised against human OSMR were screened and selected based
869 on their specificity and sensitivity in pilot immunohistochemistry assays on OSMR-
870 expressing formalin-fixed, paraffin-embedded cultured cell pellets. Two unique and
871 non-competitive clones (mAbs 604 and 605) were selected for further assay optimization
872 and staining on human tissues; both mAbs showed similar staining patterns on tissue
873 after assay optimization, so only mAb 605 staining is presented. The optimized assay
874 was performed on the Ultra Discovery Platform (Roche Diagnostics) using CC1
875 standard antigen retrieval, Discovery Antibody Block, mAb 605 diluted 3%BSA/20%
876 human serum, OmniMap anti-Rabbit-HRP, and DAB detection. Anti-Tenascin C (TNC)
877 staining was optimized on TNC-expressing formalin-fixed, paraffin-embedded cultured
878 cell pellets and human skin and glioblastoma tissues; the optimized assay was
879 performed on the Ultra Discovery Platform (Roche Diagnostics) using Protease 2
880 antigen retrieval, mAb DB7 (Abcam) diluted 3%BSA, OmniMap anti-Mouse-HRP, and
881 DAB detection. Human tissues used for OSMR staining were approved by the
882 University of California, San Francisco Institutional Review Board and adhered to the
883 principles of the Declaration of Helsinki; written informed consent was obtained from
884 all subjects. Fibrotic lung tissues were obtained at the time of lung transplantation from
885 patients with a diagnosis of usual interstitial pneumonia and normal lung tissues were
886 obtained from lungs rejected for transplantation by the Northern California Transplant
887 Donor Network. For TNC staining, all human tissues were acquired from commercial
888 sources under warranty that appropriate Institutional Review Board approval and
889 informed consent were obtained.
890
891 **Pharmacokinetic analysis of anti-mouse IL-11 study**

892 The PK of mAb418 following single i.v. dose of 10 mg/kg were conducted at Charles
893 River Laboratories, using naive female C57BL/6 mice, age 6 to 8 weeks. Blood samples
894 were collected by retro-orbital bleeds and the terminal blood sample was collected by
895 cardiac stick from each animal in each dosing group at various timepoints up to 14 days
896 post-dose with three mice per time point and processed to collect serum. Time course of
897 PK profiles and PK parameters are shown in **Extended data Fig2e.** Serum samples were
898 analyzed for test article concentrations by enzyme-linked immunosorbent assay. Mouse
899 anti-mouse IgG2a (BD Biosciences) was used as the capturing reagent and anti-mouse
900 IgG2a specific antibody conjugated to horseradish peroxidase (HRP) (GeneTex), was
901 used as the detection reagent. The serum concentration versus time data were used to
902 calculate PK parameters in mouse using noncompartmental analysis (Phoenix
903 WinNonlin, Version 6.4.0.768; Certara). Nominal sample collection times and nominal
904 dosing solution concentrations were used in the data analysis.
905
906 **ELISA/Luminex**
907 For chemokines were measured by Luminex using a MILLIPLEX MAP Mouse
908 Immunoglobulin Cytokine/Chemokine Magnetic Beat Panel (cat. no. MCYTMAG-70K-
909 PX32, Millipore).
910
911 **RNA sequencing (RNA-seq), single cell RNA-sequencing (scRNA-seq) and gene**
912 **expression analysis**
913 The concentration of total RNA samples was determined using NanoDrop 8000 (Thermo
914 Scientific) and the integrity of RNA was determined by Fragment Analyzer (Advanced
915 Analytical Technologies). 0.5 μg of total RNA was used as input material for library
916 preparation using TruSeq RNA Sample Preparation Kit v2 (Illumina). Size of the libraries
917 was confirmed using Fragment Analyzer (Advanced Analytical Technologies) and their
918 concentration was determined by a qPCR-based method using Library quantification kit
919 (KAPA). The libraries were multiplexed and then sequenced on a HiSeq2500 (Illumina)
920 to generate 30M single-end 50 base pair reads. RNA was quantified using Nanodrop 8000
921 (Thermo Scientific) and integrity was measured using the Bioanalyzer RNA 6000 Pico Kit
922 (Agilent). Libraries were prepared using the TruSeq RNA Library Prep Kit v2 (Illumina)
923 with 100-500 ng of input and amplified using 10 cycles of PCR. Libraries were
924 multiplexed and sequenced on a HiSeq 2500 System (Illumina), resulting in 15M single-

925 end 50 bp reads per library. Alignment, feature counting, normalization, and differential
926 expression analysis were performed similar to as described previously (14). In brief,
927 HTSeqGenie was used to perform filtering, alignment to GRCm38, and feature counting.
928 Normalized counts per million (CPM) values were computed as a measure of gene
929 expression. Pairwise differential expression analysis was performed using voom and
930 limma. For differential gene-expression analysis significant genes were filtered and
931 identified as Benjamini-Hochberg corrected $p < 0.05$. Pathway analysis was performed
932 with Ingenuity Pathway Analysis (IPA) software (Qiagen) using the "Diseases and
933 Disorders" pathway module. Heat map Euclidean clustering of genes was performed by
934 plotting log 2-transformed fold change values for each replicate sample and each gene
935 (log 2 floor set at -3 for heat map). Colored boxes indicate the degree of fold change. For
936 gene expression by qRT-PCR, cells or tissues were lysed using Buffer RLT (Qiagen) and
937 total RNA extracted using RNeasy Mini Kit with on-column DNase digestion (Qiagen)
938 and reverse transcribed to cDNA using iScript kit (Bio-Rad). Gene expression was
939 analyzed using TaqMan Gene Expression Assay (Applied Biosystems). *Ccl2*
940 (Mm00441242_m1), Ccr2 (Mm99999051_gH), *Cd64* (Mm00438874), *Col1a1*
941 (Mm00801666_g1), *Col1a2* (Mm00483888_m1), *Fn1* (Mm01256744_m1), *Tgfb1*
942 (Mm01178820_m1), *Arg1* (Mm00475988_m1), *Cd206* (Mm01329362_m1), *Nos2*
943 (Mm00440502) and *CCL18* (Hs00268113_m1). Target gene expression was normalized by
944 housekeeping genes *Hprt1* (Mm01545399_m1) and *Rpl19* (Mm02601633_g1) for mouse
945 transcripts, and by GAPDH (Hs02786624_g1) for human transcripts.
946
947 **Lung cell isolation for single-cell RNA sequencing**. Lungs were harvested and
948 processed in single cell suspensions such as described above, with modifications taken
949 from previous protocol optimized for single cell transcriptomics[84]. After tissue digestion,
950 RBC lysis and FcR blocking, samples were co-stained with lineage marker antibodies
951 (CD45-APC, eBioscience #17-0451-82; CD31-FITC, Biolegend #102405; EpCAM-PE,
952 Biolegend #118205), cell hashing antibodies (TotalSeq B 1-5, Biolegend) and with a
953 live/dead stain (7-AAD, BD #559925). After staining, samples were normalized in total
954 number of cells recovered, pooled per treatment group and FACS sorted to isolate
955 immune, epithelial, endothelial and stromal cell fractions.
956 **Single-cell RNA sequencing**. Sorted cell fractions were loaded on the Chromium Next
957 GEM Single Cell 3' v3.1 kit with a target of 16k cells per sample. For all samples, viabilities

958 were greater than 80% and cell concentrations ranged between 700 and 1,600 cells/ul.
959 Following the manufacturer's instructions, we loaded approximately 26400 cells into each
960 channel. Library generation was performed following the manufacturer's protocol 3' v3.1
961 with cell surface protein. Briefly, cell suspensions were encapsulated in Gel-emulsion
962 beads followed by reverse transcription. The Gel Beads-in-emulsion (GEMs) were then
963 broken open releasing the pre-amplification cDNA which was cleaned and amplified.
964 cDNA was then converted into sequencing libraries via fragmentation followed by
965 ligation of the sequencing adapters and final addition of Illumina compatible dual-index
966 primers. Libraries were sequenced on a NovaSeq 6000 according to the manufacturer's
967 specifications.
968
969 **scRNA-seq data processing and analysis**. scRNA-seq sequencing reads collected from
970 the *in vivo* anti-OSM and anti-IL6R treatment experiment were filtered and aligned using
971 cellranger v6.0.1 (10x Genomics). This data was then analyzed in the R v4.2.1 statistical
972 computing environment using the Seurat v4.2 R package[85,86]. CMO data was normalized
973 through CLR (centered-log ratio) transformation and HTO data was demultiplexed using
974 k-means clustering. Only cells with ≥ 500 genes were retained for analysis, normalization
975 was performed using the log-normalization method, and 2,000 highly-variable genes
976 were selected for sample integration and clustering using the mean/variance regression
977 method. Sample integration and batch correction was performed using the anchor-based
978 sample integration workflow. Clustering was performed using 25 PCA components on a
979 k=20 shared nearest neighbor (SNN) graph using the Louvain algorithm. UMAP
980 dimensional reductions were performed using the uwot R package. Marker selection was
981 performed using the Wilcoxon Rank Sum test on the integrated sample data for each
982 cluster against all clusters. For all analyses, percent of cells expressing a given gene
983 (detection rate) was defined as the presence of ≥ 1 UMI for the given gene. Cell type
984 annotation was performed manually based differentially expressed genes from a one-vs-
985 all comparison meeting the criteria of average log2 fold-change ≥ 0.5, a minimum
986 detection rate ≥ 20%, and either detection rate ≥ 50% within a cluster or ≤ 10% within all
987 other clusters. Withing each cell type annotations, gene counts were pseudo bulked by
988 summing count data per gene across each cell type for each mouse. Differential gene
989 expression was calculated using voom+limma with multiple-hypothesis correction of p-
990 values via the Benjamini-Hochberg method. Heatmaps were generated using the

991 pseudobulk log_2 normalized CPM expression matrix with both rows and columns
992 hierarchically clustered using Euclean distance and Ward's linkage. The top 50 most
993 variable genes that were upregulated in the BLM + Isotype vs. PBS differential
994 expression, downregulated in the BLM+aOSM+aIL6R vs. BLM+Isotype comparison,
995 with corrected $p \leq 0.05$ and had at least a 2-fold change difference between the two
996 differential expressions were plotted.
997
998 **All data sets are uploaded to GEO:** accession GSE263043

Acknowledgements

We thank members of the Wilson laboratory and Immunology Discovery department, Genentech, for discussion and reading of the manuscript and editorial assistance. The authors thank Matthew Taylor (PTPK, Genentech) and Pamela Chan (BCP, Genentech) for assistance with PK analysis. We would like to thank the vet staff at Genentech, Catherine Sohn, Dorie Montoya, Raul Garcia-Gonzalez, Emmanuel Chua, Jill Yamada, Katelyn McEachin, Ryan Scott, Fidel Guardado and Jennifer Cosino for the meticulous care and support for all animal work. We thank CK Poon, Jim Cupp, Terence Ho, Qi Xuan Tan, Andres Paler Martinez, Jovencio Borneo, Cole Meyers, Kevin Le in the FACS/Luminex laboratory for their support. We thank Jingyu Diao and Ke-Jung Huang for their initial work optimizing and performing permeability assays. We thank Alison Huynh, Jessica Mills, Sean Flanagan, Shannon Hambro, Victor Nunez, and their team for the invaluable support in animal work. We thank Andres Paler Martinez for Luminex analysis, Zhiyu Huang and Alexander Arlantico for assistance with mouse experiments, Mariela Del Rio for mouse colony management. The authors thank the Next Generation Sequencing group, Genentech, for all of their assistance, guidance, and support with RNA sequencing. We apologize to our many colleagues whose primary work could not be cited owing to space constraints.

Author Contributions

- R. A. R., E. D., H. S. D., S. H., C. J. W., R. G., G. T., D. X., conceptualized, designed, performed and analyzed a variety of experiments.
- D. R., carried out FACS staining and analysis.
- H. B.,S. J., C. L. E., A. A., A. W., S. Y., A. S., S. A., M. K. performed *in vivo* experiments.
- T. R., X. G., J. L., performed human fibroblast, epithelial and endothelial cell experiments.
- C. A., D. J. D., and P. C., performed and analyzed histology data.
- J. V. H., A. R. A., S. U., analyzed RNA-sequencing data sets.
- J. B., G. N., generated mAbs and carried out SPR studies.
- R. Y. carried out PK studies.

1030 - R. A. P., C. K-W., W. F. J., provided PCLS.
1031 - Y. S., J W., performed and analyzed OSM-induced pSTAT3 assays.
1032 - J. R. A., conceptualized experiments and edited the manuscript.
1033 - M.S.W., N. R. W., J. R. A., J. V. H., conceptualized the project, executed some
1034 experiments, wrote and edited the manuscript.
1035

1036 Funding

1037 This work was funded by Genentech Inc., Chugai Inc., and NIH grants, as below. M. K.
1038 is funded by Chugai Inc., R.A.P., C. K.-W., W. F. J., are funded by NIH grants: NCATS
1039 UL1TR003017 and NHLBI PO1HL114471. All other authors are funded by Genentech
1040 Inc.

1041 Competing interests:

1042 All authors, except R.A.P., C.K.-W., W.F.J., are current or past employees of Genentech
1043 Inc., a member of the Roche group, and may hold Roche stock or stock options. C.K.-W.
1044 is a co-editor in chief for Current Research in Pharmacology and Drug Discovery.

Figure 1.

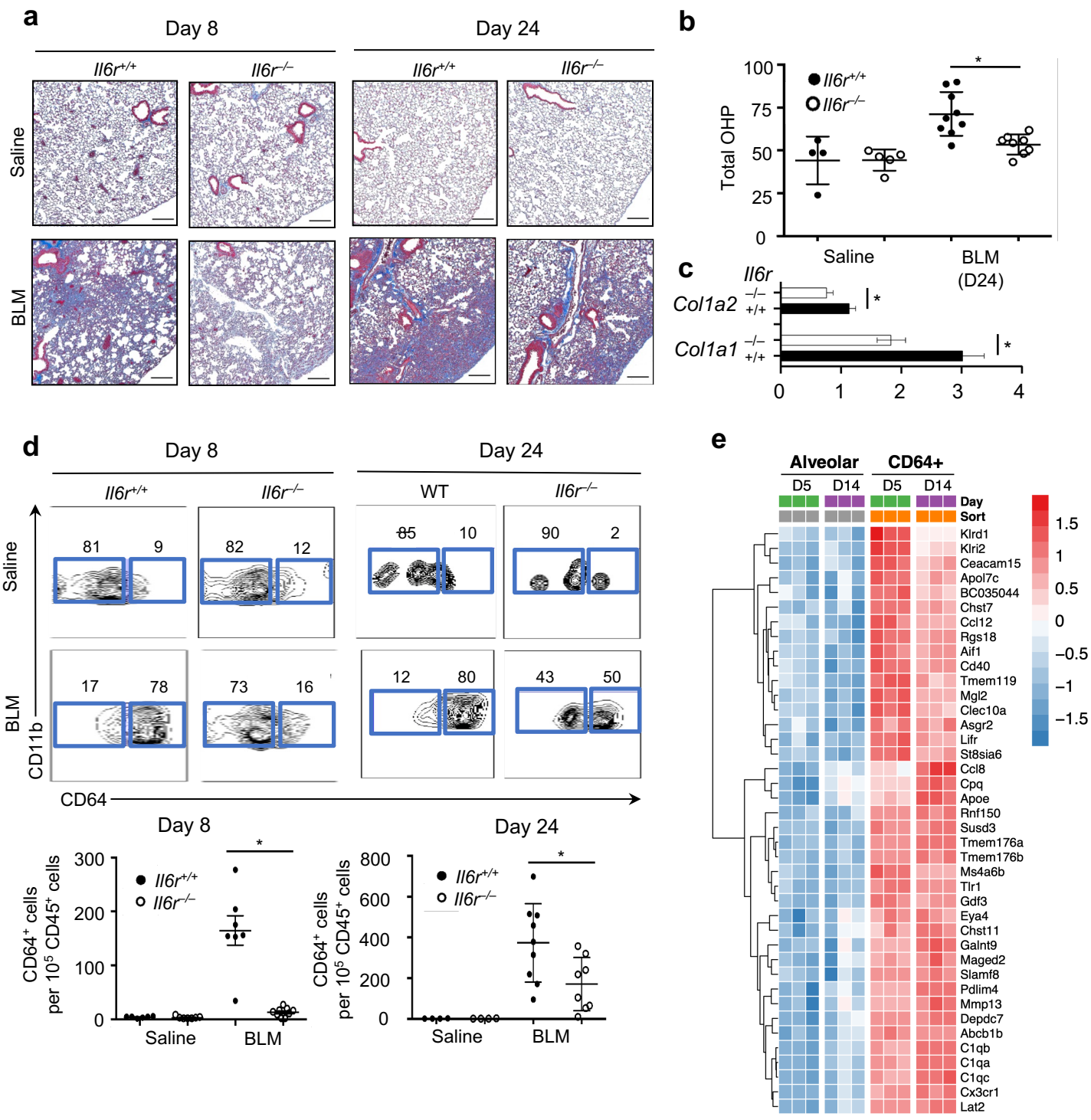
a
Day 8
Day 24
Il6r+/+
Il6r−/−
Saline
BLM
b
Total OHP
100
75
50
25
0
Il6r+/+
Il6r−/−
*
Saline
BLM
(D24)
c
Il6r
Col1a2
Col1a1
−/−
+/+
*
0
1
2
3
4
d
Day 8
Day 24
Il6r+/+
Il6r−/−
WT
Saline
BLM
81
9
82
12
85
10
90
2
17
78
73
16
12
80
43
50
CD11b
CD64
CD64+ cells per 10^5 CD45+ cells
300
200
100
0
800
600
400
200
0
Saline
BLM
e
Alveolar
CD64+
D5
D14
D5
D14
Day
Sort
Klrd1
Klri2
Ceacam15
Apol7c
BC035044
Chst7
Ccl12
Rgs18
Aif1
Cd40
Tmem119
Mgl2
Clec10a
Asgr2
Lifr
St8sia6
Ccl8
Cpq
Apoe
Rnf150
Susd3
Tmem176a
Tmem176b
Ms4a6b
Tlr1
Gdf3
Eya4
Chst11
Galnt9
Maged2
Slamf8
Pdlim4
Mmp13
Depdc7
Abcb1b
C1qb
C1qa
C1qc
Cx3cr1
Lat2
1.5
1
0.5
0
−0.5
−1
−1.5

1045 **Figure. 1.**

1046 **IL-6 dependent CD64$^+$ macrophage populations drive fibrotic disease.**

1047 a. WT (*Il6r*$^{+/+}$) and IL-6-deficient (*Il6r*$^{-/-}$) mice were given intratracheal saline or
1048 bleomycin (BLM) on day 0, 2 and 4, as described in methods. Masson's Trichrome
1049 stained lung tissue at day 8 and day 24 post BLM was carried out to identify
1050 collagen deposition. 4-8 mice per group, representative images shown.

1051 b. Total hydroxyproline (Total OHP, ug/half lung) lung tissue was measured at day
1052 24. 4-8 mice per group. P value calculated by t-test. Graphs show mean ± SD. *
1053 $P<0.05$.

1054 c. Gene expression measured in lung tissue by qRT-PCR. 4-8 mice per group. P value
1055 calculated by t-test. Graphs show mean ± SD. * $P<0.05$.

1056 d. FACS analysis of lung tissue at day 8 and day 24 from saline or BLM treated WT
1057 (*Il6r*$^{+/+}$) and IL-6-deficient (*Il6r*$^{-/-}$) mice showing representative FACS plots (top) and
1058 numbers of CD64$^+$ macrophages (CD45$^+$CD11c$^+$SigF$^+$MHCII$^+$CD11b$^+$CD64$^+$) per 10^5
1059 CD45$^+$ cells (bottom). 4-8 mice per group. P value calculated by t-test. Graphs show
1060 mean ± SD. * $P<0.05$.

1061 e. Heatmap showing the top 40 (by fold-change) differentially expressed genes (DEG)
1062 in alveolar macrophages (CD45$^+$CD11c$^+$SigF$^-$) and CD64$^+$ macrophages
1063 (CD45$^+$CD11c$^+$SigF$^-$MHCII$^+$CD11b$^+$CD64$^+$) macrophages from WT mice treated with
1064 saline or BLM at day 5 or day 14.

Figure 2.

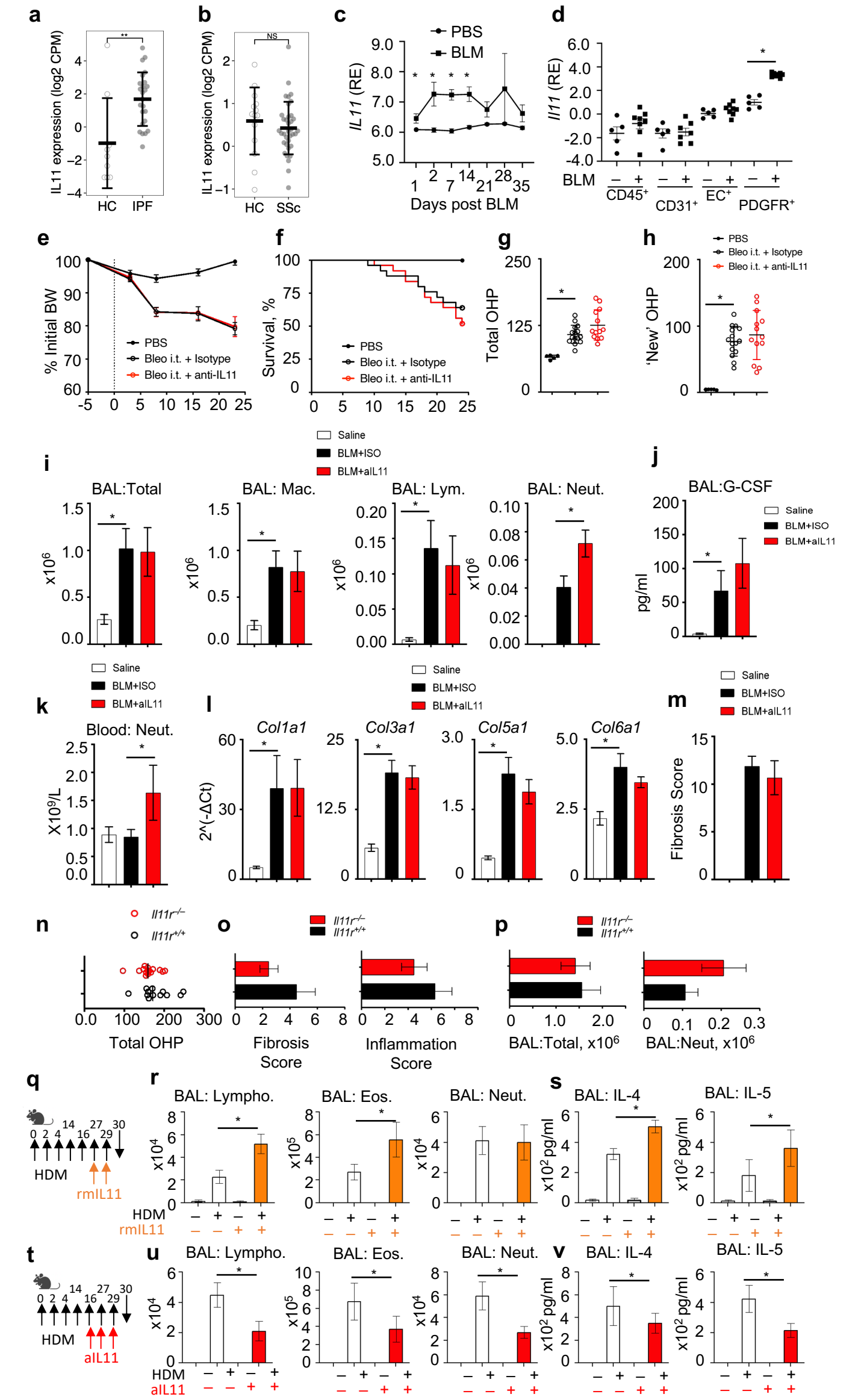
a
IL11 expression (log2 CPM)
HC
IPF
b
IL11 expression (log2 CPM)
HC
SSc
NS
c
PBS
BLM
IL11 (RE)
Days post BLM
d
Il11 (RE)
BLM
CD45+
CD31+
EC+
PDGFR+
e
% Initial BW
PBS
Bleo i.t. + Isotype
Bleo i.t. + anti-IL11
f
Survival, %
PBS
Bleo i.t. + Isotype
Bleo i.t. + anti-IL11
g
Total OHP
h
'New' OHP
PBS
Bleo i.t. + Isotype
Bleo i.t. + anti-IL11
Saline
BLM+ISO
BLM+aIL11
i
BAL:Total
BAL: Mac.
BAL: Lym.
BAL: Neut.
x10^6
j
BAL:G-CSF
pg/ml
k
Blood: Neut.
X10^9/L
l
Col1a1
Col3a1
Col5a1
Col6a1
2^(-ΔCt)
m
Fibrosis Score
n
Il11r-/-
Il11r+/+
Total OHP
o
Fibrosis Score
Inflammation Score
p
BAL:Total, x10^6
BAL:Neut, x10^6
q
HDM
rmIL11
r
BAL: Lympho.
BAL: Eos.
BAL: Neut.
s
BAL: IL-4
BAL: IL-5
t
HDM
aIL11
u
BAL: Lympho.
BAL: Eos.
BAL: Neut.
v
BAL: IL-4
BAL: IL-5

1065 **Figure 2.**

1066 **Redundant, pathogenic and protective roles of IL-11 in lung, liver and kidney.**

1067 a. Lung biopsies were obtained from healthy controls (n=9) and IPF patients (n=24),
1068 RNA-seq was carried out and *IL11* transcripts analyzed. Graphs show log_2
1069 normalized CPM, mean ± SD. * FDR P<0.05, ** FDR P<0.005; NS not significant.

1070 b. Skin biopsies obtained from healthy controls (n=14) and SSc patients (n=36),
1071 participating in the focuSSced clinical trial, RNA-seq was carried out and *IL11*
1072 transcripts analyzed. Graphs show log_2 normalized CPM, mean ± SD. * FDR
1073 P<0.05, ** FDR P<0.005; NS not significant.

1074 c. WT C57BL/6J mice were given intratracheal saline (PBS) or bleomycin (BLM) on
1075 day 0, 2 and 4, as described in methods. Lung tissue was collected on day 1, 2, 7,
1076 14, 21, 28 and 35 post BLM. RNA was extracted and *Il11* transcripts determined
1077 by RNA sequencing. N = 5-25 mice per group. Graphs show mean ± SD. * P<0.05
1078 at each time point.

1079 d. WT C57BL/6J mice were given intratracheal saline (PBS) or bleomycin (BLM) on
1080 day 0, 2 and 4, as described in methods. Lung tissue was collected on day 24 post
1081 BLM. Lung tissue was dissociated for FACS staining and sorting. $CD45^+$ $CD31^+$,
1082 $Epcam^+$ and $PDGFR^+$ cells were purified, with RNA extracted for RNA
1083 sequencing. N = 3, 5-10 mice per pooled group. Graphs show mean ± SD. *
1084 P<0.05.

1085 e. WT C57BL/6J mice were given intratracheal saline (PBS) or bleomycin (BLM) on
1086 day 0, 2 and 4, as described in methods. Mice were given anti-IL-11 mAb
1087 (MAB418, 20mg/kg every 3 days, from day -1). Body weight was monitored
1088 weekly.

1089 f. Survival was monitored and mice with >25% weight loss were euthanized.

1090 g. Total hydroxyproline (Total OHP, ug/half lung) in lung tissue was measured at
1091 day 24. 5-25 mice per group. P value calculated by t-test. Graphs show mean ±
1092 SD. * P<0.05.

1093 h. 'New' hydroxyproline (New OHP, ug/half lung) in lung tissue was measured in
1094 deuterated water treated mice, as described in methods, at day 24. 5-25 mice per
1095 group. P value calculated by t-test. Graphs show mean ± SD. * P<0.05.

1096 i. Bronchoalveolar lavage (BAL) was performed on mice at day 24, as described in
1097 methods. Total and differential cell counts (Macrophages, Mac; Lymphocytes,

1098 Lym; Neutrophils, Neut) were determined from each mouse. 5-25 mice per
1099 group. P value calculated by t-test. Graphs show mean ± SD. * P<0.05.
1100 j. Bronchoalveolar lavage (BAL) was performed on mice at day 24, as described in
1101 methods. GCSF was measured by Luminex. 5-25 mice per group. P value
1102 calculated by t-test. Graphs show mean ± SD. * P<0.05.
1103 k. Whole blood was collected from mice at day 24. WBC and differential cell
1104 analysis was measured on a Cobas system. 5-25 mice per group. P value
1105 calculated by t-test. Graphs show mean ± SD. * P<0.05.
1106 l. Gene expression measured in lung tissue by qRT-PCR. 5-25 mice per group. P
1107 value calculated by t-test. Graphs show mean ± SD. * P<0.05.
1108 m. Lung pathology (fibrosis score) was assessed in a blinded manner, as described
1109 in methods.
1110 n. WT (*Il11r*$^{+/+}$) and IL-11R-deficient (*Il11r*$^{-/-}$) C57BL/6J mice were given
1111 intratracheal saline (PBS) or bleomycin (BLM) on day 0, 2 and 4, as described in
1112 methods. Total hydroxyproline (Total OHP, ug/half lung) in lung tissue was
1113 measured at day 24. 10 mice per group. P value calculated by t-test. Graphs show
1114 mean ± SD. * P<0.05.
1115 o. Lung pathology (fibrosis score and inflammation score) was assessed in a
1116 blinded manner, as described in methods. 10 mice per group. P value calculated
1117 by t-test. Graphs show mean ± SD. * P<0.05.
1118 p. Bronchoalveolar lavage (BAL) was performed on mice at day 24, as described in
1119 methods. Total and neutrophil cell counts were determined from each mouse. 10
1120 mice per group. P value calculated by t-test. Graphs show mean ± SD. * P<0.05.
1121 q. C57BL/6 mice were treated with 10ug HDM in 25ul via the intratracheal route
1122 on day 0, 2, 4, 14, 16, 27, 29, 30. Mice were also given rmIL-11 via the
1123 intratracheal route, as indicated and described in methods, on day 27 and 29.
1124 Mice were analyzed for airway inflammation on day 30.
1125 r. Bronchoalveolar lavage (BAL) was performed on mice at day 24, as described in
1126 methods. Total and differential cell counts (Lymphocytes, Lym; Neutrophils,
1127 Neut; Eosinophils, Eos) were determined from each mouse. 5-15 mice per group.
1128 P value calculated by t-test. Graphs show mean ± SD. * P<0.05.

1129 s. Bronchoalveolar lavage (BAL) was performed on mice at day 30, as described in
1130 methods. IL-4 and IL-5 was measured by Luminex. 5-15 mice per group. P value
1131 calculated by t-test. Graphs show mean ± SD. * P<0.05.
1132 t. C57BL/6 mice were treated with 10ug HDM in 25ul via the intratracheal route
1133 on day 0, 2, 4, 14, 16, 27, 29, 30. Mice were also given anti-mouse IL-11 mAbs i.p.,
1134 as indicated and described in methods, on day 16, 27 and 29. Mice were analyzed
1135 for airway inflammation on day 30.
1136 u. Bronchoalveolar lavage (BAL) was performed on mice at day 24, as described in
1137 methods. Total and differential cell counts (Lymphocytes, Lym; Neutrophils,
1138 Neut; Eosinophils, Eos) were determined from each mouse. 5-15 mice per group.
1139 P value calculated by t-test. Graphs show mean ± SD. * P<0.05.
1140 v. Bronchoalveolar lavage (BAL) was performed on mice at day 30, as described in
1141 methods. IL-4 and IL-5 was measured by Luminex. 5-15 mice per group. P value
1142 calculated by t-test. Graphs show mean ± SD. * P<0.05.

Figure 3.

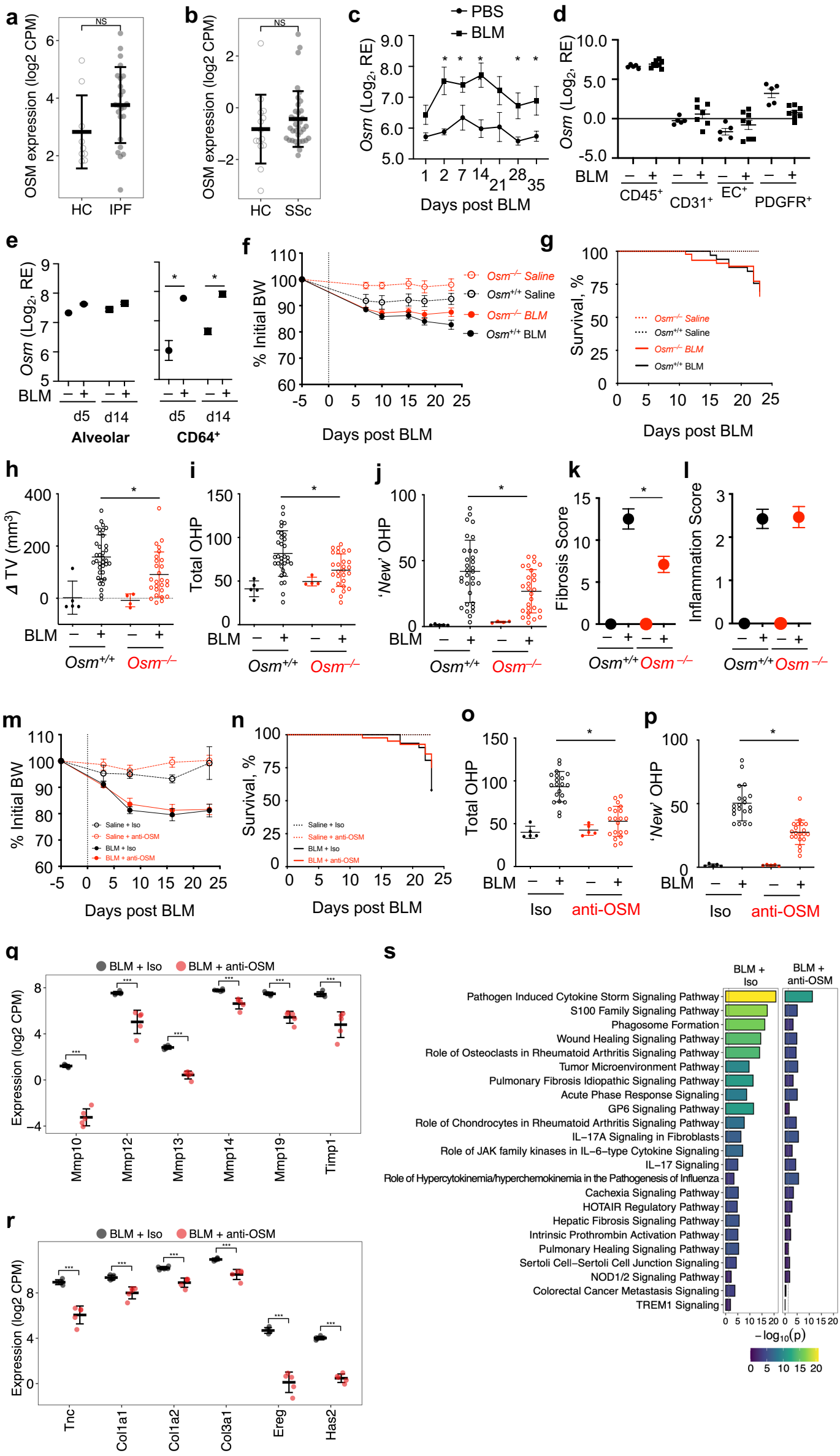
a
OSM expression (log2 CPM)
NS
HC
IPF
b
OSM expression (log2 CPM)
NS
HC
SSc
c
PBS
BLM
Osm (Log2, RE)
Days post BLM
d
Osm (Log2, RE)
BLM
CD45+
CD31+
EC+
PDGFR+
e
Osm (Log2, RE)
BLM
d5
d14
Alveolar
CD64+
f
% Initial BW
Osm−/− Saline
Osm+/+ Saline
Osm−/− BLM
Osm+/+ BLM
Days post BLM
g
Survival, %
Osm−/− Saline
Osm+/+ Saline
Osm−/− BLM
Osm+/+ BLM
Days post BLM
h
Δ TV (mm3)
BLM
Osm+/+
Osm−/−
i
Total OHP
BLM
Osm+/+
Osm−/−
j
'New' OHP
BLM
Osm+/+
Osm−/−
k
Fibrosis Score
Osm+/+
Osm−/−
l
Inflammation Score
Osm+/+
Osm−/−
m
% Initial BW
Saline + Iso
Saline + anti-OSM
BLM + Iso
BLM + anti-OSM
Days post BLM
n
Survival, %
Saline + Iso
Saline + anti-OSM
BLM + Iso
BLM + anti-OSM
Days post BLM
o
Total OHP
BLM
Iso
anti-OSM
p
'New' OHP
BLM
Iso
anti-OSM
q
BLM + Iso
BLM + anti-OSM
Expression (log2 CPM)
Mmp10
Mmp12
Mmp13
Mmp14
Mmp19
Timp1
r
BLM + Iso
BLM + anti-OSM
Expression (log2 CPM)
Tnc
Col1a1
Col1a2
Col3a1
Ereg
Has2
s
BLM + Iso
BLM + anti-OSM
Pathogen Induced Cytokine Storm Signaling Pathway
S100 Family Signaling Pathway
Phagosome Formation
Wound Healing Signaling Pathway
Role of Osteoclasts in Rheumatoid Arthritis Signaling Pathway
Tumor Microenvironment Pathway
Pulmonary Fibrosis Idiopathic Signaling Pathway
Acute Phase Response Signaling
GP6 Signaling Pathway
Role of Chondrocytes in Rheumatoid Arthritis Signaling Pathway
IL−17A Signaling in Fibroblasts
Role of JAK family kinases in IL−6−type Cytokine Signaling
IL−17 Signaling
Role of Hypercytokinemia/hyperchemokinemia in the Pathogenesis of Influenza
Cachexia Signaling Pathway
HOTAIR Regulatory Pathway
Hepatic Fibrosis Signaling Pathway
Intrinsic Prothrombin Activation Pathway
Pulmonary Healing Signaling Pathway
Sertoli Cell−Sertoli Cell Junction Signaling
NOD1/2 Signaling Pathway
Colorectal Cancer Metastasis Signaling
TREM1 Signaling
−log10(p)

1143 **Figure 3.**

1144 **Significant and non-redundant role of Oncostatin M (OSM) in pulmonary fibrosis.**

1145 a. Lung biopsies were obtained from healthy controls (n=9) and IPF patients (n=24),
1146 RNA-seq was carried out and *OSM* transcripts analyzed. Graphs show $\log_2$
1147 normalized CPM, mean ± SD. * FDR P<0.05, ** FDR P<0.005; NS not significant.

1148 b. Skin biopsies obtained from healthy controls (n=14) and SSc patients (n=36)
1149 participating in the focuSSced clinical trial and *OSM* transcripts measured.
1150 Graphs show $\log_2$ normalized CPM, mean ± SD. * FDR P<0.05, ** FDR P<0.005;
1151 NS not significant.

1152 c. WT C57BL/6J mice were given intratracheal saline (PBS) or bleomycin (BLM) on
1153 day 0, 2 and 4, as described in methods. Lung tissue was collected on day 1, 2, 7,
1154 14, 21, 28 and 35 post BLM. RNA was extracted and *Osm* transcripts determined
1155 by RNA sequencing. N = 5-25 mice per group. Graphs show mean ± SD. * P<0.05
1156 at each time point.

1157 d. WT C57BL/6J mice were given intratracheal saline (PBS) or bleomycin (BLM) on
1158 day 0, 2 and 4, as described in methods. Lung tissue was collected on day 24 post
1159 BLM. Lung tissue was dissociated for FACS staining and sorting. $CD45^+$ $CD31^+$,
1160 $Epcam^+$ and $PDGFR^+$ cells were purified, with RNA extracted for RNA
1161 sequencing. N = 3, 5-10 mice per pooled group. Graphs show mean ± SD. *
1162 P<0.05.

1163 e. *Osm* expression in alveolar macrophages ($CD45^+CD11c^+SigF^-$) and $CD64^+$
1164 macrophages ($CD45^+CD11c^+SigF^-MHCII^+CD11b^+CD64^+$) macrophages from WT
1165 mice treated with saline or BLM at day 5 or day 14. N = 3, 5-10 mice per pooled
1166 group. Graphs show mean ± SD. * P<0.05.

1167 f. WT ($Osm^{+/+}$) and OSM-deficient ($Osm^{-/-}$) C57BL/6J mice were given intratracheal
1168 saline (PBS) or bleomycin (BLM) on day 0, 2 and 4, as described in methods.
1169 Body weight was monitored weekly and expressed as % of initial weight.

1170 g. Survival was monitored and mice with >25% weight loss were euthanized.

1171 h. Tissue volume (TV) was determined at day 22, as described in methods.

1172 i. Total hydroxyproline (Total OHP, ug/half lung) in lung tissue was measured at
1173 day 24. 5-25 mice per group. P value calculated by t-test. Graphs show mean ±
1174 SD. * P<0.05.

1175 j. 'New' hydroxyproline (New OHP, ug/half lung) in lung tissue was measured in
1176 deuterated water treated mice, as described in methods, at day 24. 5-25 mice per
1177 group. P value calculated by t-test. Graphs show mean ± SD. * P<0.05.
1178 k. Lung pathology (fibrosis score) was assessed in a blinded manner, as described
1179 in methods. 5-25 mice per group. P value calculated by t-test. Graphs show mean
1180 ± SD. * P<0.05.
1181 l. Lung pathology (inflammation score) was assessed in a blinded manner, as
1182 described in methods. 5-25 mice per group. P value calculated by t-test. Graphs
1183 show mean ± SD. * P<0.05.
1184 m. WT C57BL/6J mice were given intratracheal saline (PBS) or bleomycin (BLM) on
1185 day 0, 2 and 4, as described in methods. Mice were given anti-OSM mAb
1186 (500ug/mouse every 3 days, from day -1). Body weight was monitored weekly.
1187 n. Survival was monitored and mice with >25% weight loss were euthanized.
1188 o. Total hydroxyproline (Total OHP, ug/half lung) in lung tissue was measured at
1189 day 24. 5-25 mice per group. P value calculated by t-test. Graphs show mean ±
1190 SD. * P<0.05.
1191 p. 'New' hydroxyproline (New OHP, ug/half lung) in lung tissue was measured in
1192 deuterated water treated mice, as described in methods, at day 24. 5-25 mice per
1193 group. P value calculated by t-test. Graphs show mean ± SD. * P<0.05.
1194 q. Lung tissue was recovered from mice at day 14 post BLM. RNA was extracted
1195 and used for RNA sequencing. Disease-relevant, tissue remodeling gene
1196 expression are shown for anti-OSM treated and isotype control mice. Graphs
1197 show individual mice with crossbars indicating mean ± standard deviation. ***
1198 FDR P<0.0005.
1199 r. Disease-relevant, fibrosis-related genes are shown for anti-OSM treated and
1200 isotype control mice. Graphs show individual mice with mean with crossbars
1201 indicating mean ± standard deviation. *** FDR P<0.0005.
1202 s. Top Ingenuity pathway analyses (IPA) are shown for isotype and anti-OSM
1203 treated mice following BLM.

Figure 4.

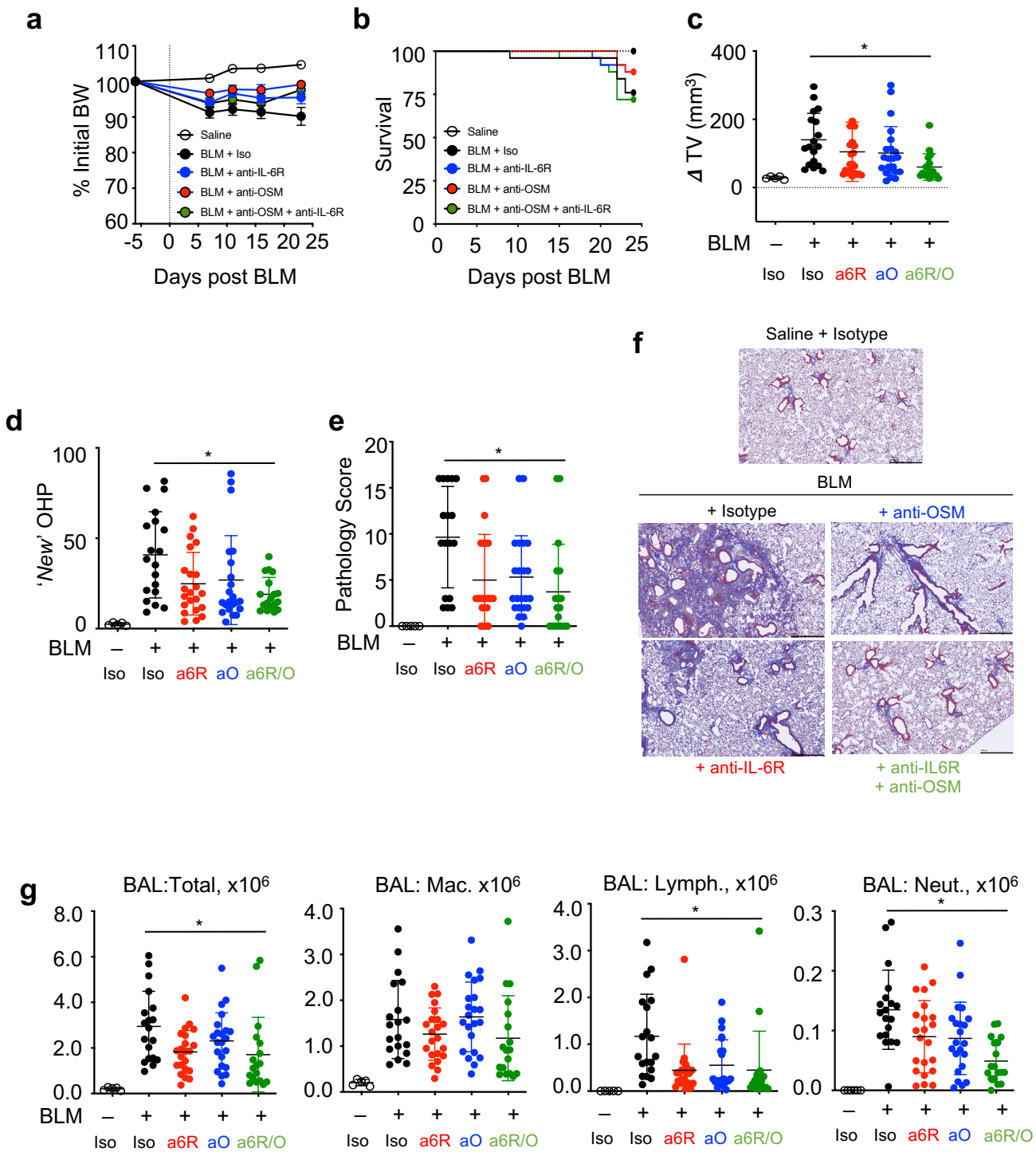
a
% Initial BW
Days post BLM
Saline
BLM + Iso
BLM + anti-IL-6R
BLM + anti-OSM
BLM + anti-OSM + anti-IL-6R
b
Survival
Days post BLM
c
Δ TV (mm³)
BLM
Iso Iso a6R aO a6R/O
d
'New' OHP
e
Pathology Score
f
Saline + Isotype
BLM
+ Isotype
+ anti-OSM
+ anti-IL-6R
+ anti-IL6R
+ anti-OSM
g
BAL:Total, x10⁶
BAL: Mac. x10⁶
BAL: Lymph., x10⁶
BAL: Neut., x10⁶

1204 **Figure 4.**

1205 **Combined IL6 and OSM antagonism significantly reduces lung injury, inflammation**
1206 **and fibrosis.**

1207 a. WT C57BL/6J mice were given intratracheal saline (PBS) or bleomycin (BLM) on
1208 day 0, 2 and 4, as described in methods. Mice were given anti-OSM mAb +
1209 isotype, anti-IL-6R mAb + isotype, or anti-IL-6R + anti-OSMR mAb
1210 (500ug/mouse every 3 days, from day -1). Body weight was monitored weekly.
1211 5-25 mice per group. P value calculated by t-test. Graphs show mean ± SD. *
1212 P<0.05.
1213 b. Survival was monitored and mice with >25% weight loss were euthanized.
1214 c. Tissue volume (TV) was determined at day 22, as described in methods. 5-25
1215 mice per group. P value calculated by t-test. Graphs show mean ± SD. * P<0.05.
1216 d. 'New' hydroxyproline (New OHP, ug/half lung) in lung tissue was measured in
1217 deuterated water treated mice, as described in methods, at day 24. 5-25 mice per
1218 group. P value calculated by t-test. Graphs show mean ± SD. * P<0.05.
1219 e. Lung pathology (fibrosis score) was assessed in a blinded manner, as described
1220 in methods. 5-25 mice per group. P value calculated by t-test. Graphs show
1221 individual mice and mean ± SD. * P<0.05.
1222 f. Lung tissue was recovered at day 24 for sectioning and assessment of pathology.
1223 Representative masons trichrome stained sections shown.
1224 g. Bronchoalveolar lavage (BAL) was performed on mice at day 24, as described in
1225 methods. Total and differential cell counts (Macrophages, Mac; Lymphocytes,
1226 Lym; Neutrophils, Neut) were determined from each mouse. 5-25 mice per
1227 group. P value calculated by t-test. Graphs show mean ± SD. * P<0.05.

Figure 5.

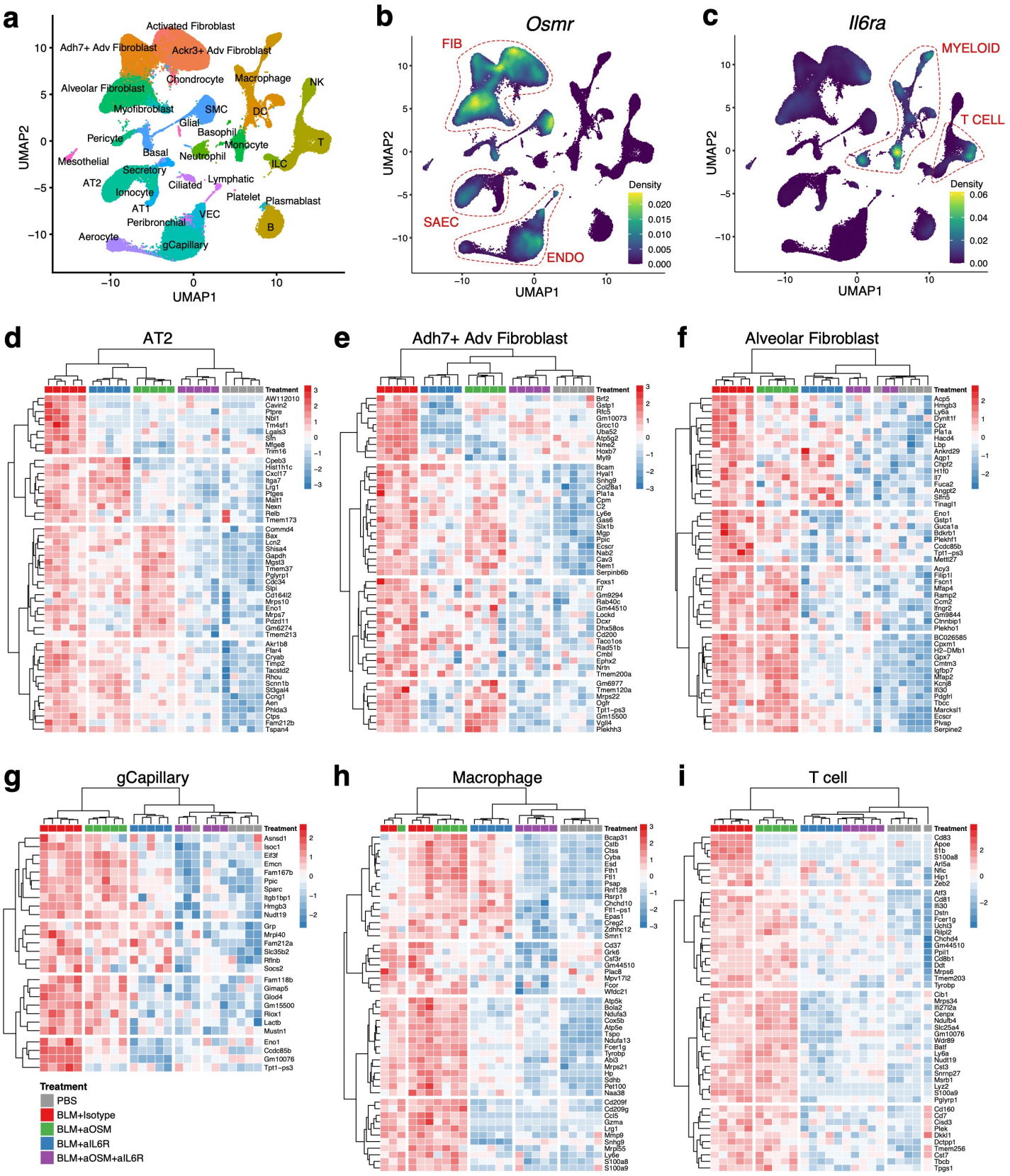
a
Activated Fibroblast
Adh7+ Adv Fibroblast
Ackr3+ Adv Fibroblast
Chondrocyte
Macrophage
NK
Alveolar Fibroblast
Myofibroblast
SMC
DC
Glial
Basophil
Pericyte
Monocyte
T
Mesothelial
Basal
Neutrophil
ILC
Secretory
Lymphatic
AT2
Ciliated
Ionocyte
Platelet
Plasmablast
AT1
VEC
Peribronchial
B
Aerocyte
gCapillary
UMAP1
UMAP2
b
Osmr
FIB
SAEC
ENDO
Density
c
Il6ra
MYELOID
T CELL
d
AT2
e
Adh7+ Adv Fibroblast
f
Alveolar Fibroblast
g
gCapillary
h
Macrophage
i
T cell
Treatment
PBS
BLM+Isotype
BLM+aOSM
BLM+aIL6R
BLM+aOSM+aIL6R

1228 **Figure 5.**

1229 **Combined IL6 and OSM antagonism has broad impact on single lung cell**
1230 **transcriptional responses in BLM treated mice.**

1231 Lung tissue was recovered from mice at day 24 post-BLM, digested and dissociated and
1232 used for single cell RNA sequencing and analysis.

1233 a. UMAP showing cellular populations recovered and identified.
1234 b. UMAP showing *Osmr* expression density across cells.
1235 c. UMAP showing *Il6r*a expression density across cells.

1236 Hierarchical clustered heatmap showing genes (FDR <= 0.05) that were both
1237 upregulated in disease (BLM + Isotype (red treatment group, far left) vs. PBS (grey
1238 treatment group, far right) and down regulated in combination (BLM + anti-OSM +
1239 anti-IL-R6 (purple treatment group) vs. disease (BLM + Isotype (red treatment group).
1240 Individual treatment groups (anti-IL-6R (blue treatment group) and anti-OSM (green
1241 treatment group) are shown to identify impact of monotherapy.

1242 d. Genes in SAEC (AT2 cluster) shown.
1243 e. Genes in adventitial fibroblasts (Adh7+ Adv Fibroblast cluster) shown.
1244 f. Genes in alveolar fibroblasts (Alveolar Fibroblast cluster) shown.
1245 g. Genes in endothelial cells (gCapillary cluster) shown.
1246 h. Genes in macrophages (Macrophage cluster) shown.
1247 i. Genes in T cells (T cluster) shown.

Figure 6.

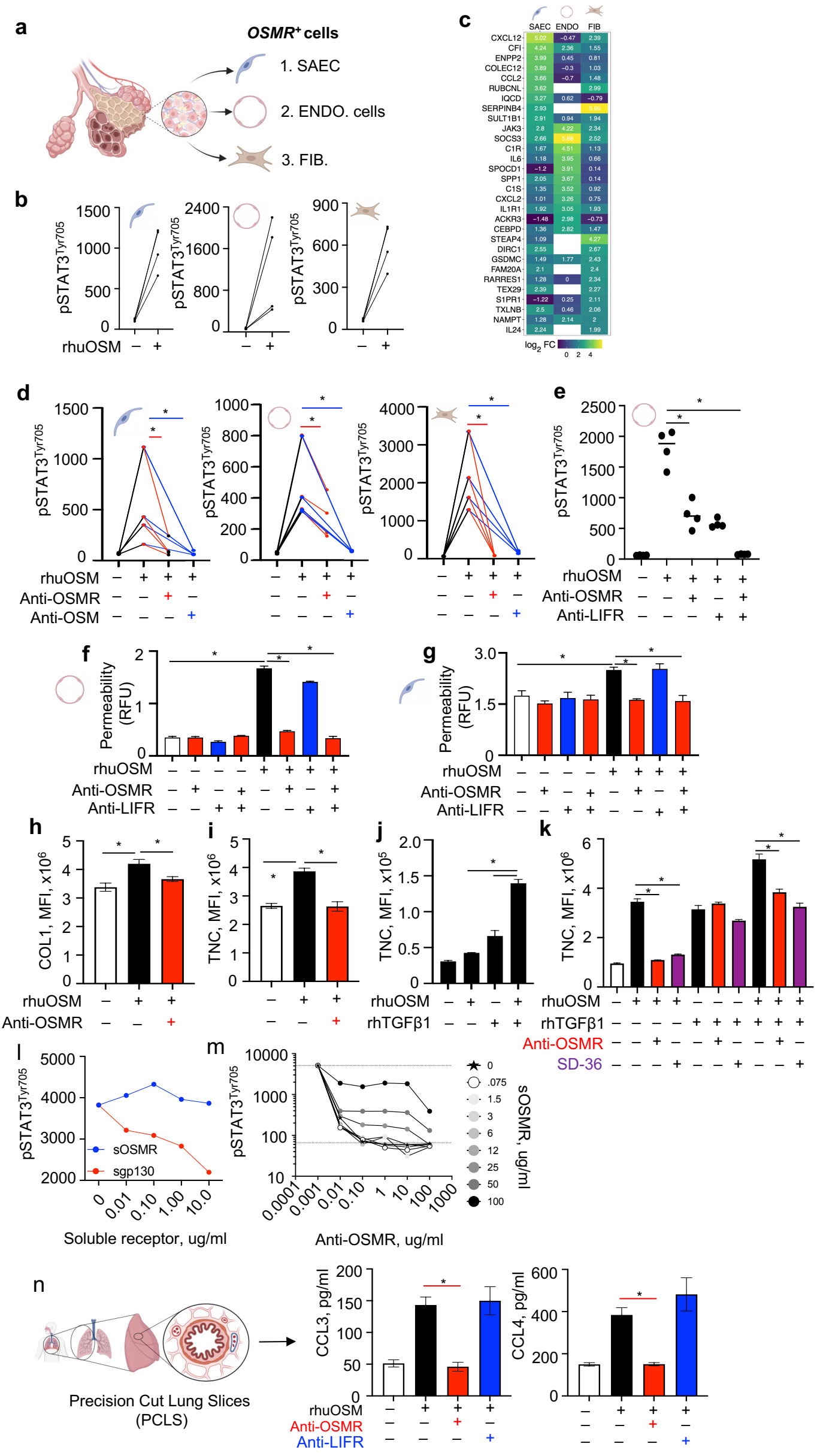
a
OSMR+ cells
1. SAEC
2. ENDO. cells
3. FIB.
b
pSTAT3Tyr705
rhuOSM
c
SAEC ENDO FIB
CXCL12 5.02 −0.47 2.39
CFI 4.24 2.36 1.55
ENPP2 3.99 0.45 0.81
COLEC12 3.89 −0.3 1.03
CCL2 3.66 −0.7 1.48
RUBCNL 3.62 2.99
IQCD 3.27 0.62 −0.79
SERPINB4 2.93 5.95
SULT1B1 2.91 0.94 1.94
JAK3 2.8 4.22 2.34
SOCS3 2.66 5.88 2.52
C1R 1.67 4.51 1.13
IL6 1.18 3.95 0.66
SPOCD1 −1.2 3.91 0.14
SPP1 2.05 3.67 0.14
C1S 1.35 3.52 0.92
CXCL2 1.01 3.26 0.75
IL1R1 1.92 3.05 1.93
ACKR3 −1.48 2.98 −0.73
CEBPD 1.36 2.82 1.47
STEAP4 1.09 4.27
DIRC1 2.55 2.67
GSDMC 1.49 1.77 2.43
FAM20A 2.1 2.4
RARRES1 1.28 0 2.34
TEX29 2.39 2.27
S1PR1 −1.22 0.25 2.11
TXLNB 2.5 0.46 2.06
NAMPT 1.28 2.14 2
IL24 2.24 1.99
log2 FC
d
pSTAT3Tyr705
rhuOSM
Anti-OSMR
Anti-OSM
e
pSTAT3Tyr705
rhuOSM
Anti-OSMR
Anti-LIFR
f
Permeability (RFU)
rhuOSM
Anti-OSMR
Anti-LIFR
g
Permeability (RFU)
rhuOSM
Anti-OSMR
Anti-LIFR
h
COL1, MFI, x10^6
rhuOSM
Anti-OSMR
i
TNC, MFI, x10^6
j
TNC, MFI, x10^5
rhuOSM
rhTGFβ1
k
TNC, MFI, x10^6
rhuOSM
rhTGFβ1
Anti-OSMR
SD-36
l
pSTAT3Tyr705
sOSMR
sgp130
Soluble receptor, ug/ml
m
pSTAT3Tyr705
sOSMR, ug/ml
Anti-OSMR, ug/ml
n
Precision Cut Lung Slices (PCLS)
CCL3, pg/ml
CCL4, pg/ml
rhuOSM
Anti-OSMR
Anti-LIFR

1248 **Figure 6.**

1249 **OSM mediates disease-relevant pathogenic responses in epithelial, endothelial cells**
1250 **and fibroblasts in an OSMR-dependent manner.**

1251 a. Graphic showing OSMR-expressing shows identified from human scRNA-seq.
1252 Small airway epithelia cells (SAEC), endothelial (ENDO) cells and Fibroblasts
1253 (FIB).
1254 b. Primary human SAEC, ENDO or FIB were cultured, as described in methods,
1255 and stimulated with rhOSM (10ng/ml) for 15 mins. Cell lysates were recovered
1256 and $pSTAT3^{Tyr705}$ was measured by MSD.
1257 c. Primary human SAEC, ENDO or FIB were cultured, as described in methods,
1258 and stimulated with rhOSM (10ng/ml) for 24hrs. RNA was extracted for RNA
1259 seq analysis. Top 10 differentially expressed genes (FDR P<0.05) are shown for
1260 each cell type. LogFC values shown in boxes.
1261 d. Primary human SAEC, ENDO or FIB were cultured, as described in methods,
1262 and stimulated with rhOSM (10ng/ml) for 15 mins. Cells were either treated
1263 with anti-OSMR (50ug/ml) or anti-OSM (10ug/ml) from 120 mins prior to OSM
1264 treatment. Cell lysates were recovered and $pSTAT3^{Tyr705}$ was measured by MSD.
1265 P value calculated by t-test. Graphs show mean ± SD. * P<0.05.
1266 e. Primary human ENDO cells were cultured, as described in methods, and
1267 stimulated with rhOSM (10ng/ml) for 15 mins. Cells were either treated with
1268 anti-OSMR (50ug/ml) or anti-LIFR (50ug/ml) from 120 mins prior to OSM
1269 treatment. Cell lysates were recovered and $pSTAT3^{Tyr705}$ was measured by MSD.
1270 P value calculated by t-test. Graphs show mean ± SD. * P<0.05.
1271 f. Primary human ENDO cells were cultured, as described in methods, and
1272 permeability was assessed following rhOSM (10ng/ml) treatment. Cells were
1273 either treated with anti-OSMR (50ug/ml) or anti-LIFR (50ug/ml) from 120 mins
1274 prior to OSM treatment. P value calculated by t-test. Graphs show mean ± SD. *
1275 P<0.05.
1276 g. Primary human SAEC were cultured, as described in methods, and permeability
1277 was assessed following rhOSM (10ng/ml) treatment. Cells were either treated
1278 with anti-OSMR (50ug/ml) or anti-LIFR (50ug/ml) from 120 mins prior to OSM
1279 treatment. P value calculated by t-test. Graphs show mean ± SD. * P<0.05.

1280 h. Primary human FIB cells were cultured, as described in methods, and stimulated
1281 with rhOSM (10ng/ml) for 72 hrs. Cells were treated with anti-OSMR (50ug/ml)
1282 or anti-LIFR (50ug/ml) from 120 mins prior to OSM treatment. Collagen (COL)
1283 secretion was stained and assessed using CellInsight CX7, in the scar-in-a-jar
1284 assay, as described in methods. P value calculated by t-test. Graphs show mean ±
1285 SD. * P<0.05.
1286 i. Primary human FIB cells were cultured, as described in methods, and stimulated
1287 with rhOSM (10ng/ml) for 72 hrs. Cells were treated with anti-OSMR (50ug/ml)
1288 anti-LIFR (50ug/ml) from 120 mins prior to OSM treatment. Tenascin C (TNC)
1289 secretion was stained and assessed using CellInsight CX7, in the scar-in-a-jar
1290 assay, as described in methods. P value calculated by t-test. Graphs show mean ±
1291 SD. * P<0.05.
1292 j. Primary human FIB cells were cultured, as described in methods, and stimulated
1293 with rhOSM (10ng/ml) or rhTGFβ (1ng/ml) for 72 hrs. Tenascin C (TNC)
1294 secretion was stained and assessed using CellInsight CX7, in the scar-in-a-jar
1295 assay, as described in methods. P value calculated by t-test. Graphs show mean ±
1296 SD. * P<0.05.
1297 k. Primary human FIB cells were cultured, as described in methods, and stimulated
1298 with rhOSM (10ng/ml) or rhTGFβ (1ng/ml) for 72 hrs. Cells were treated with
1299 anti-OSMR (50ug/ml) or SD-36 (10⌈M), as indicated, from 120 mins prior to OSM
1300 treatment. Tenascin C (TNC) secretion was stained and assessed using
1301 CellInsight CX7, in the scar-in-a-jar assay, as described in methods. P value
1302 calculated by t-test. Graphs show mean ± SD. * P<0.05.
1303 l. Primary human FIB cells were cultured, as described in methods, and stimulated
1304 with rhOSM (10ng/ml) for 15 mins. Cells were treated with either soluble OSMR
1305 (sOSMR) or soluble gp130 (sgp130) at indicated concentrations from 120 mins
1306 prior to OSM treatment. Cell lysates were recovered and $pSTAT3^{Tyr705}$ was
1307 measured by MSD.
1308 m. Primary human FIB cells were cultured, as described in methods, and stimulated
1309 with rhOSM (10ng/ml) for 15 mins. Cells were treated with soluble OSMR
1310 (sOSMR) and anti-OSMR at indicated concentrations from 120 mins prior to

1311 OSM treatment. Cell lysates were recovered and pSTAT3^{Tyr705} was measured by
1312 MSD.
1313 n. Precision cut lung slices (PCLS) were prepared, as described in methods, and
1314 stimulated with rhOSM (10ng/ml) for 24hrs with anti-OSMR (50ug/ml) or anti-
1315 LIFR (50ug/ml) from 120 mins prior to OSM treatment and throughout. CCL3
1316 and CCL4 were measured by luminex in supernatants. P value calculated by t-
1317 test. Graphs show mean ± SD. * $P<0.05$.

Extended Data 1.

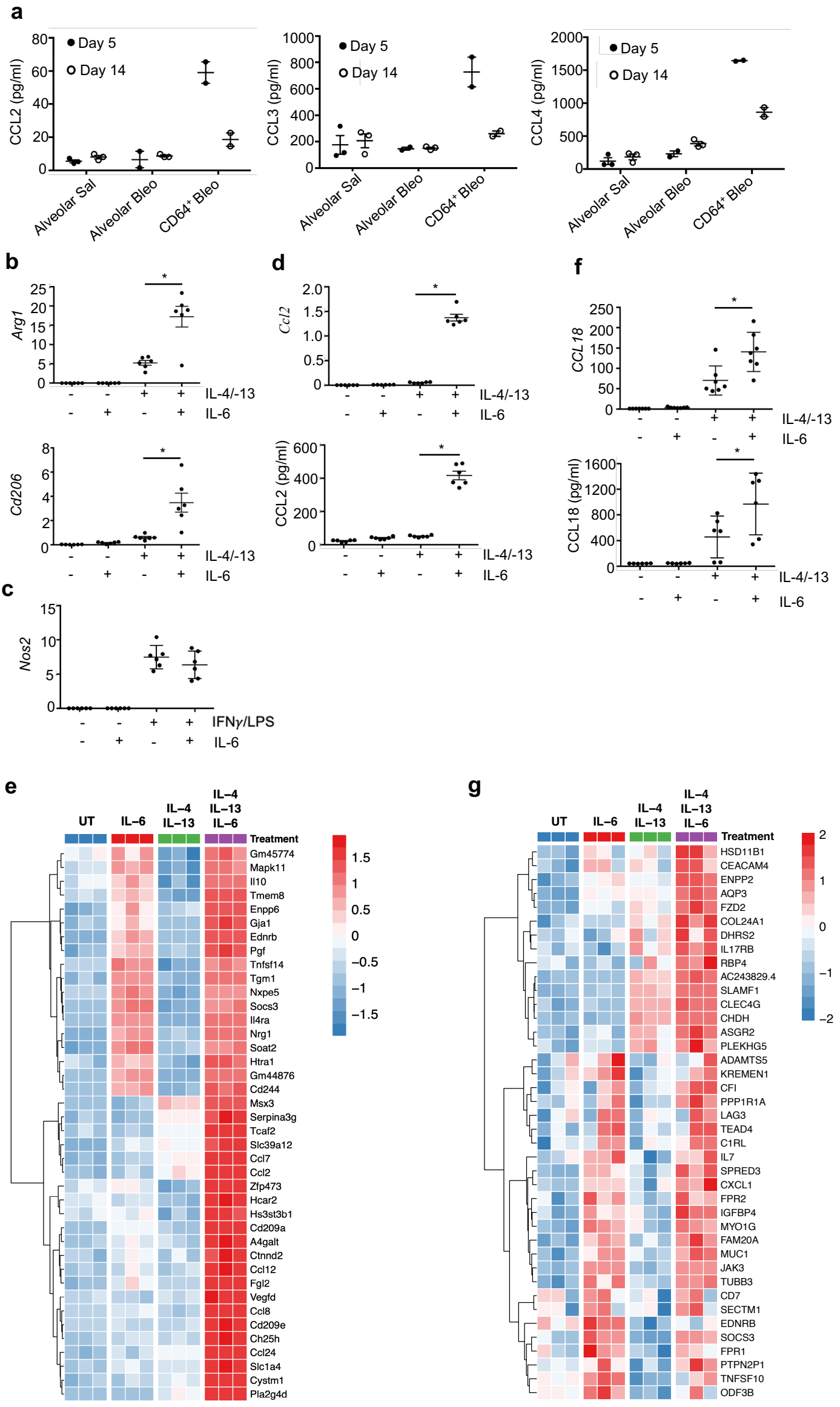

1318 **Extended Data 1.**

1319 **IL-6 activates myeloid cells and drives inflammatory and fibrotic programs.**

1320 a. Alveolar macrophages ($CD45^+CD11c^+SigF^+$) and $CD64^+$ ($CD45^+CD11c^+SigF^-$
1321 $MHCII^+CD11b^+CD64^+$) macrophages were FACS sorted from the lungs of WT
1322 mice 5 and 14 days post BLM treatment. Sorted cells were then placed in culture
1323 for 24 hours and CCL2, CCL3 and CCL4 was analyzed using Luminex. Graphs
1324 show mean of two independent experiments ± SD. * P<0.05.

1325 b. WT BMDMs were treated with IL-4 and IL-13 +/– IL-6 for 24 hours before gene
1326 expression analysis was assessed by qRT-PCR (n=6). Graphs show mean ± SD. *
1327 P<0.05.

1328 c. WT BMDMs were treated with IFN© and LPS +/– IL-6 for 24 hours before gene
1329 expression analysis was assessed by qRT-PCR (n=6). Graphs show mean ± SD. *
1330 P<0.05.

1331 d. WT BMDMs were treated with IL-4 and IL-13 +/– IL-6 for 24 hours with CCL2
1332 measured in supernatant by Luminex and gene expression assessed by qRT-PCR
1333 (n=6). Graphs show mean ± SD. * P<0.05.

1334 e. WT BMDMs were treated with IL-4 and IL-13 +/– IL-6 for 24 hours before RNA
1335 was extracted for RNA-sequencing. Heat map showing the most differentially
1336 upregulated genes between untreated and IL-4 + IL-13 +IL-6 treatment across all
1337 treatment groups (top 40 by fold change and adjusted P value <0.05, n=3).

1338 f. Monocyte derived macrophages (MDMs) were generated from healthy donors
1339 and polarized with IL-4 and IL-13 +/– IL-6 for 24 hours. CCL18 mRNA and
1340 protein was measured using qRT-PCR and ELISA, respectively (n=7). Graphs
1341 show mean ± SD. * P<0.05.

1342 g. Monocyte derived macrophages (MDMs) were generated from healthy donors
1343 and polarized with IL-4 and IL-13 +/– IL-6 for 24 hours. RNA was extracted for
1344 RNA sequencing. Heatmap showing the most differentially upregulated genes
1345 are between untreated and IL-4 + IL-13 +IL-6 treatment across all treatment
1346 groups (top 40 by fold change, adjusted p<0.05, n=3).

Extended Data 2.

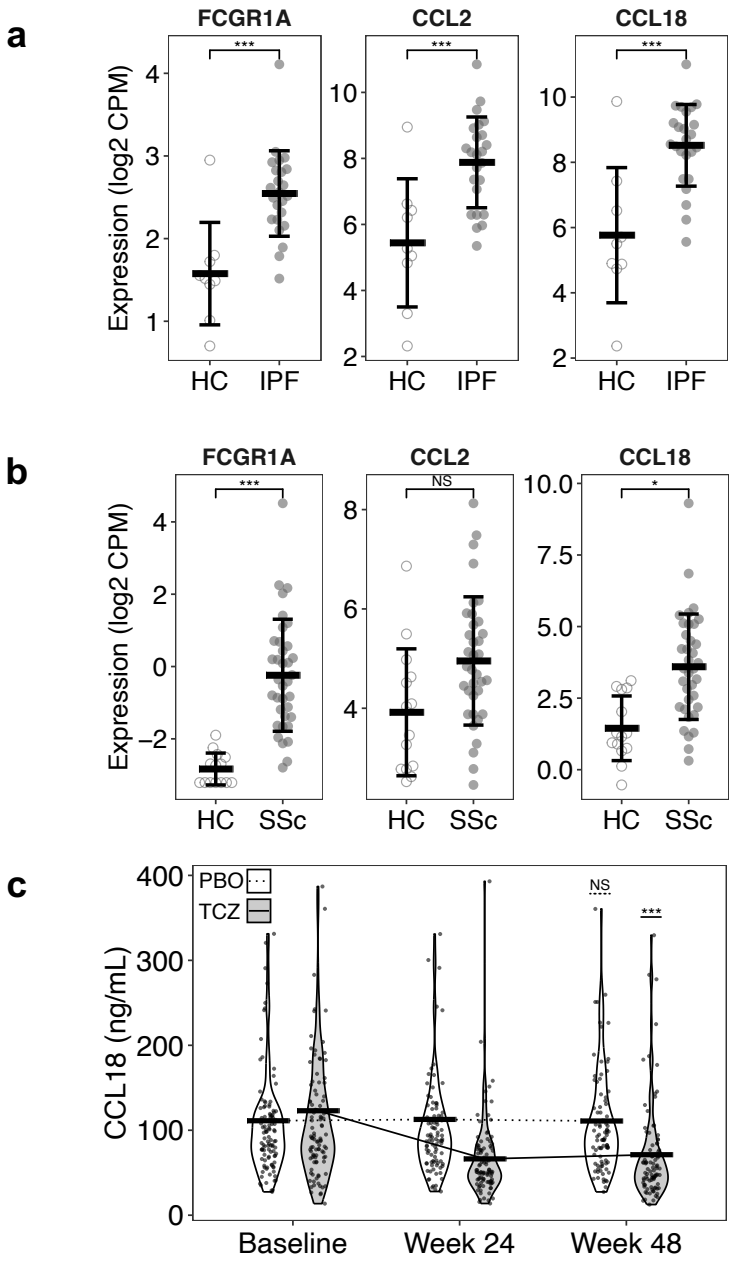

1347 **Extended Data 2.**

1348 **Correlates of IL-6-driven responses in human IPF lung and SSc skin and IL-6-dependnet**
1349 **CCL18 in serum.**

1350 a. Lung biopsies were obtained from healthy controls (n=9) and IPF patients
1351 (n=24), RNA-seq was carried out and *FCGR1A (CD64), CCL2* and *CCL18*
1352 transcripts analyzed. Graphs show normalized log2 CPM, mean ± SD.
1353 ***P<0.0005, NS not significant.

1354 b. Skin biopsies obtained from healthy controls (n=14) and SSc patients (n=36)
1355 participating in the focuSSced clinical trial and *FCGR1A (CD64), CCL2* and
1356 *CCL18* transcripts measured at baseline. Graphs show normalized log2 CPM,
1357 mean ± SD. * P<0.05, ***P<0.0005, NS not significant.

1358 c. Serum was obtained from SSc patients (n=207) participating in the focuSSced
1359 clinical trial and serum CCL18 was measured at baseline and after 24 or 48
1360 weeks of PBO (n=104) or TCZ (n=103) treatment. P values calculated by t-
1361 tests between baseline and week 48. Graphs show ng/mL and mean (bar). ***
1362 P<0.0005, NS not significant.

1363

1364

Extended Data 3.

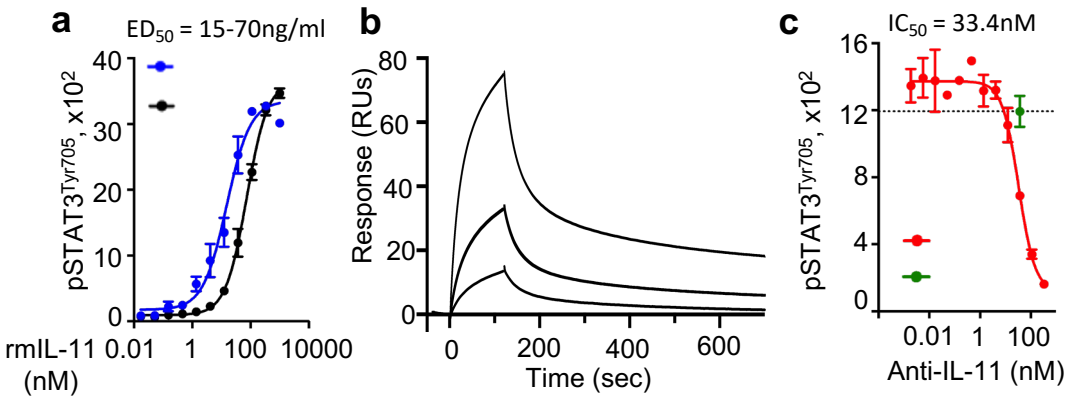

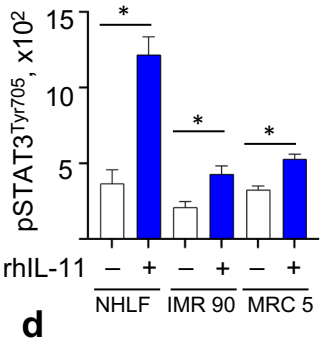

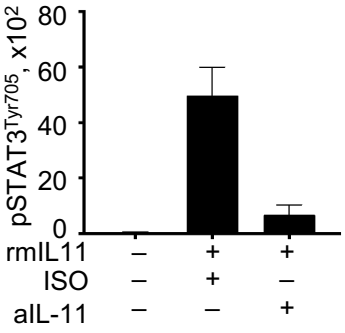

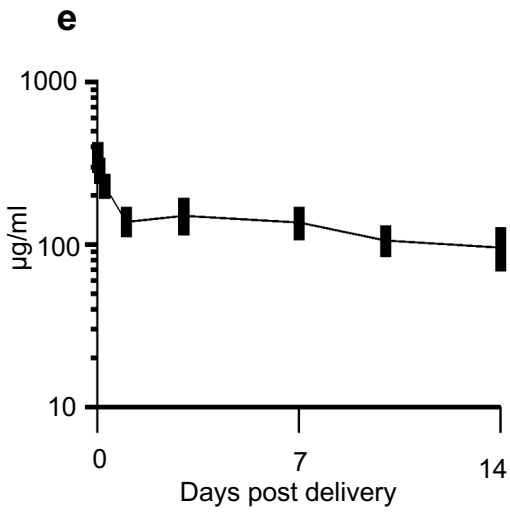

Molecule	Anti-IL-11
Dose, Route	10 mg/kg, IV
Cmax (ug/mL) ± SE	351 ± 11.9
AUC_last (ug/mL*day) ± SE	1841.5 ± 46.5
CL (mL/day/kg)	2.9
Vss (mL/kg)	67.3
$T_{1/2}$ (day)	15.8

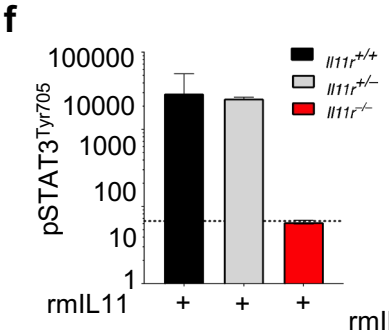

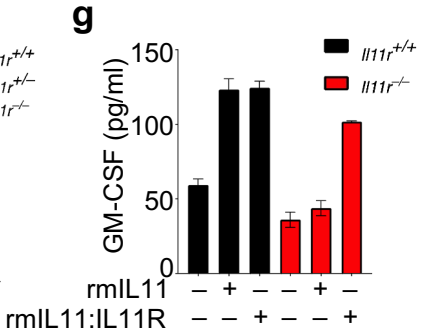

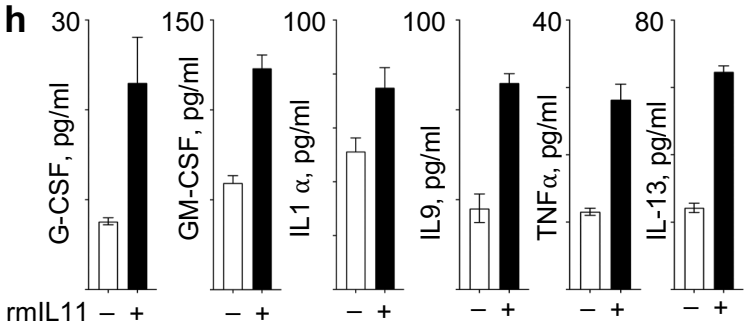

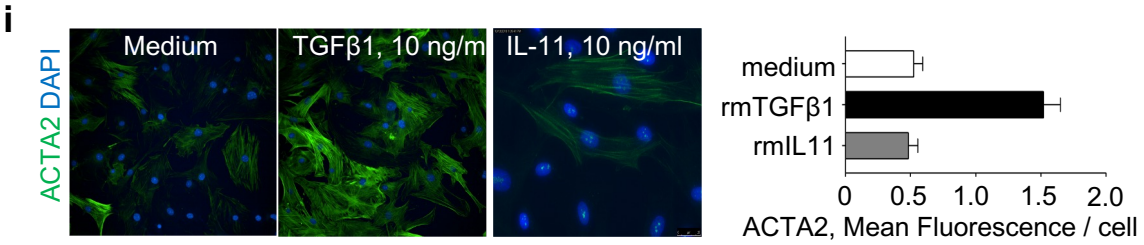

1365 **Extended Data 3.**

1366 **IL-11 mediated activation of STAT3 and induction of inflammatory cytokines, but**
1367 **not α–SMA.**

1368 a. Murine LGg cells were stimulated with increasing concentrations of rmIL-11
1369 from two different sources (murine, top, blue= R&D systems, black= in house
1370 generated, human, bottom, R&D systems). pSTAT3^{Tyr705} was measured by MSD
1371 after 15 mins. Primary human normal lung fibroblasts (NHLF) of fibroblast cell
1372 lines (IMR 90, MRC 5) were stimulated with rhIL-11 (10ng/ml). pSTAT3^{Tyr705} was
1373 measured by MSD after 15 mins.

1374 b. Binding kinetics of anti-mouse IL-11 (MAB418) determined using surface
1375 plasmon resonance (SPR).

1376 c. *In vitro* inhibition of IL-11-induced pSTAT3^{Tyr705} by anti-mouse IL-11 (MAB418,
1377 red line) or isotype rat IgG (green). IC_{50} = 33.4nM. pSTAT3^{Tyr705} was measured by
1378 MSD after 15 mins.

1379 d. *In vivo* inhibition of IL-11-induced pSTAT3^{Tyr705} by anti-mouse IL-11 (MAB418).
1380 Mice were treated with anti-IL-11 (250ug) on day 0. On day 1 mice were given
1381 25ng of rmIL-11 via the intra tracheal route. After 15 mins, mice were euthanized
1382 and whole lungs removed. pSTAT3^{Tyr705} was measured by MSD after 15 mins in
1383 whole lung lysate.

1384 e. Pharmacokinetic (PK) properties of anti-IL-11 were characterized following a
1385 single intravenous (IV) dose of 10 mg/kg in female C57BL/6 mice.

1386 f. Primary mouse lung-derived fibroblasts were isolated from *Il11*$^{+/+}$, *Il11*$^{+/-}$ and
1387 *Il11*$^{-/-}$ mice and stimulated with rm-IL-11 (10ng/ml). pSTAT3^{Tyr705} was measured
1388 by MSD after 15 mins.

1389 g. Primary mouse lung-derived fibroblasts were isolated from *Il11*$^{+/+}$ and *Il11*$^{-/-}$
1390 mice and stimulated with rm-IL-11 (10ng/ml) or rmIL-11 fused with IL-11R.
1391 After 24 hrs., GM-CSF secretion was measured by luminex. One of 3 experiments
1392 shown.

1393 h. Primary mouse lung-derived fibroblasts were isolated from WT mice and
1394 stimulated with rmIL-11 (10ng/ml). Cytokine and growth factor secretions were
1395 measured by Luminex after 24hrs.

1396 i. Primary mouse lung-derived fibroblasts were isolated from WT mice and
1397 stimulated with rmTGFβ (10ng/ml) or rmIL-11 (10ng/ml). ACTA2 (⟨SMA) was
1398 measured after 72hrs by immunofluorescence.

Extended Data 4.

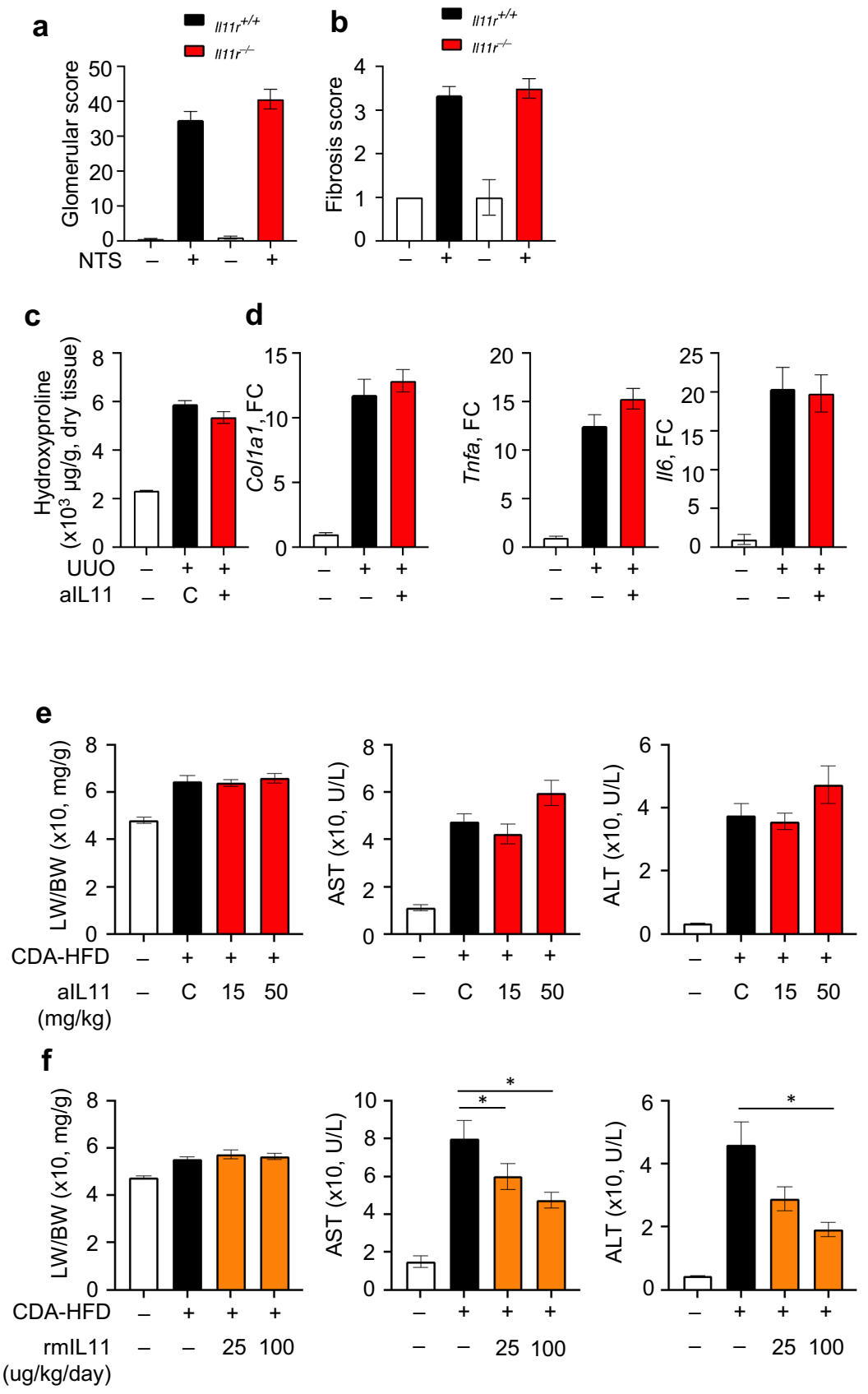

1399 **Extended Data 4.**

1400 **IL-11 is not required for experimental kidney fibrosis or liver damage.**

1401 a. WT (*Il11r*$^{+/+}$) and IL-11R-deficient (*Il11r*$^{-/-}$) C57BL/6J mice were exposed to
1402 nephrotoxic serum (NTS), as described in methods. Glomerular score as
1403 described in methods, was assessed in a blinded manner on day 42.

1404 b. Kidney fibrosis, as described in methods, was assessed in a blinded manner on
1405 day 42.

1406 c. WT C57BL/6J mice underwent UUO surgery, as described in methods. Mice
1407 were given isotype control Ab (C) or 50mg/kg of anti-mouse IL-11 (aIL11, Clone
1408 5A6) one day before surgery. Hydroxyproline (ug/g dry tissue) was assessed on
1409 day 7.

1410 d. Gene expression was measured in homogenized kidney tissue on day 7 post-
1411 surgery.

1412 e. WT C57BL/6J mice were fed a **Choline-deficient, L-amino acid-defined, high-**
1413 **fat diet** (CDA-HFD) *ad libitum*. 5P75 was the normal diet. Mice were treated with
1414 isotype control Ab (C), 25mg/kg or 50mg/kg of anti-mouse IL-11 (clone 5A6) on
1415 day 0 and day 7. Liver weight to body weight ratio, serum AST and serum ALT
1416 was measured on day 14.

1417 f. WT C57BL/6J mice were fed a CDA-HFD as above. Mice were given saline or
1418 rmIL-11 (25 or 100ug/kg/day, R&D) from day 7-11 and assessed at day 14.

Extended Data 5.

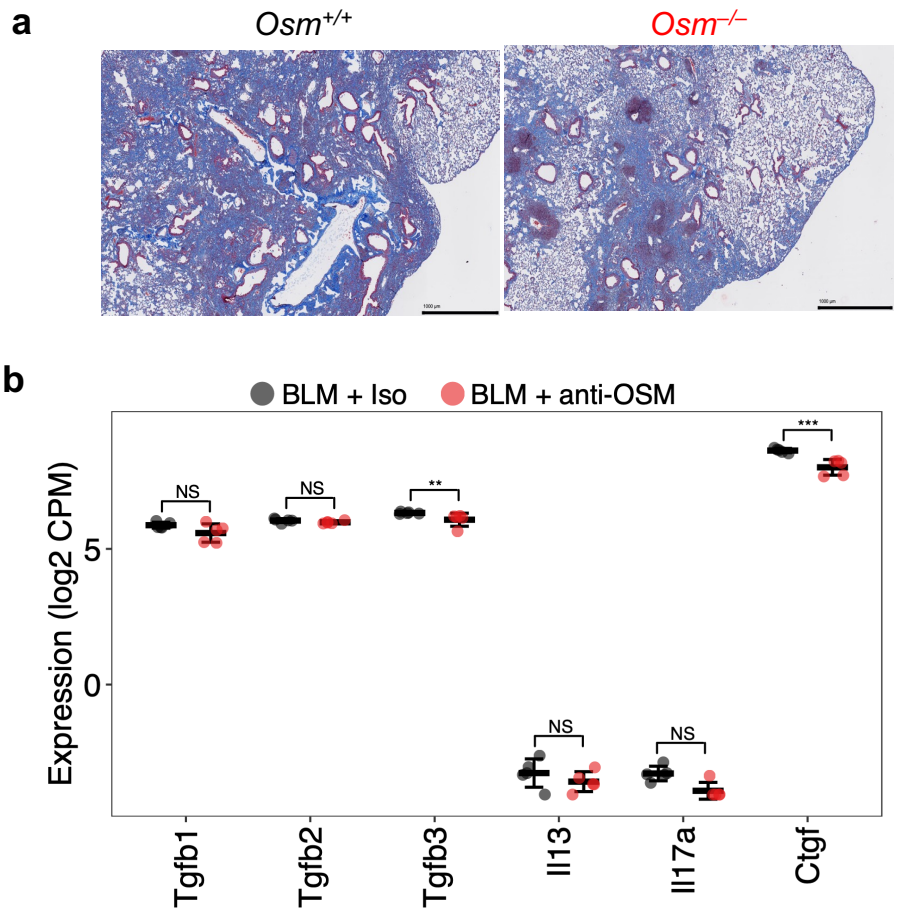

1419 **Extended data 5.**

1420 **Oncostatin M (OSM) antagonism reduces tissue fibrosis, but not canonical pro-**
1421 **fibrotic cytokines or growth factors.**

1422 a. WT (*Osm*$^{+/+}$) and OSM-deficient (*Osm*$^{-/-}$) C57BL/6J mice were given
1423 intratracheal saline (PBS) or bleomycin (BLM) on day 0, 2 and 4, as described
1424 in methods. Lung tissue was recovered at day 24 for sectioning and
1425 assessment of pathology. Representative masons trichrome stained sections
1426 shown.

1427 b. Lung tissue was recovered from mice at day 14 post BLM. RNA was extracted
1428 and used for RNA sequencing. Disease-relevant, pro-fibrotic cytokines and
1429 growth factor genes are shown for anti-OSM treated and isotype control mice.
1430 Graphs show individual mice with crossbar indicating mean ± standard
1431 deviation. NS not significant, ** FDR P<0.005, *** P<0.0005.

Extended Data 6.

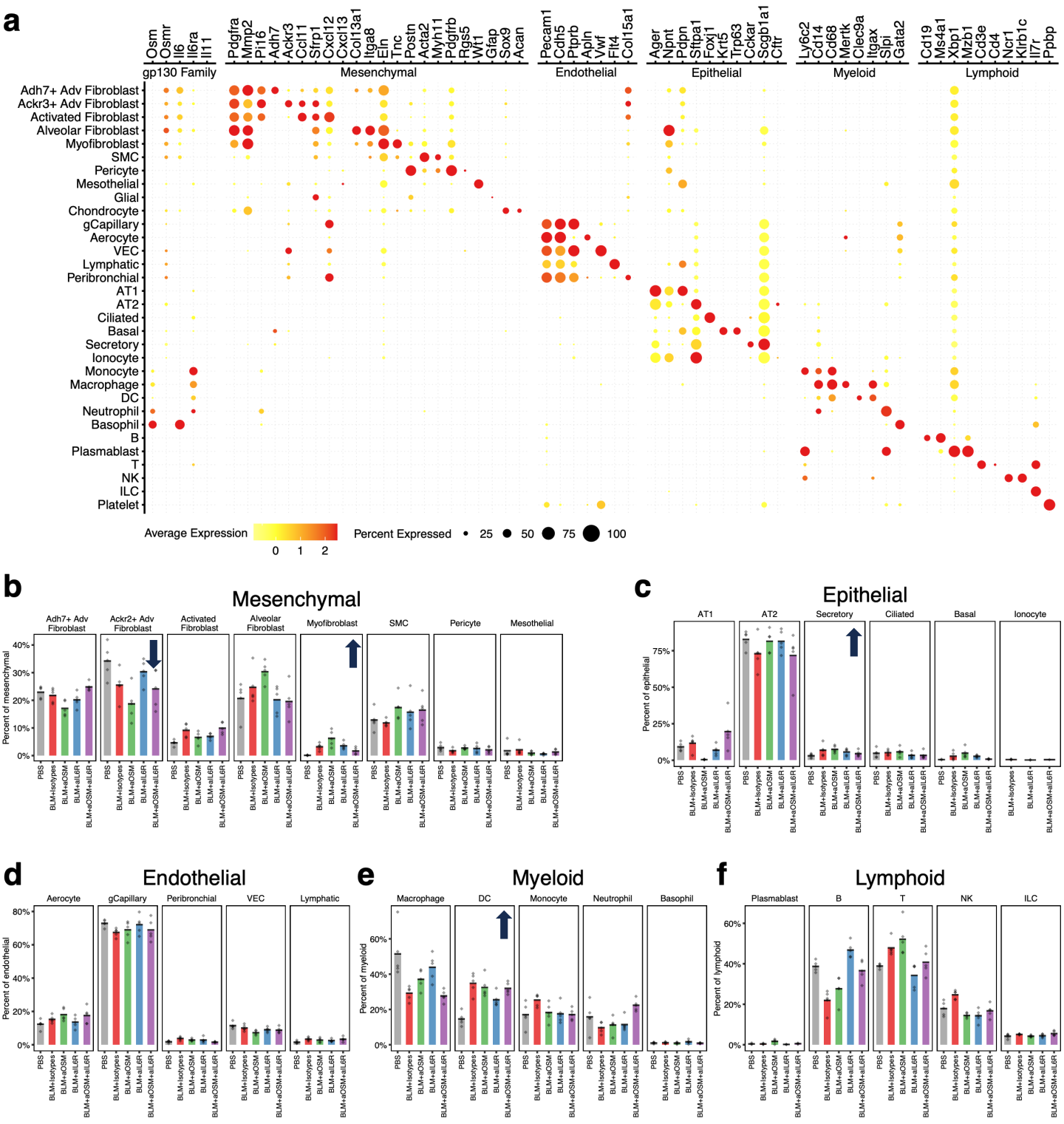

1432 **Extended data 6.**

1433 **Lung cell transcriptional identities and profiles and proportional changes following**
1434 **BLM and mAb treatment.**

1435 Lung tissue was recovered from mice at day 24 post-BLM, digested and dissociated and
1436 used for single cell RNA sequencing and analysis.

1437 a. Dot plot showing cell identities (left) and representative gene expression. Size of
1438 dot refers to percentage of cells expressing gene and color refers to average
1439 expression.
1440 b. Proportional shifts in mesenchymal cell populations following BLM and mAb
1441 treatment for individual mice (points) and mean (bar height).
1442 c. Proportional shifts in epithelial cell populations following BLM and mAb
1443 treatment for individual mice (points) and mean (bar height).
1444 d. Proportional shifts in endothelial cell populations following BLM and mAb
1445 treatment for individual mice (points) and mean (bar height).
1446 e. Proportional shifts in myeloid cell populations following BLM and mAb
1447 treatment for individual mice (points) and mean (bar height).
1448 f. Proportional shifts in lymphoid cell populations following BLM and mAb
1449 treatment for individual mice (points) and mean (bar height).

Extended Data 7.

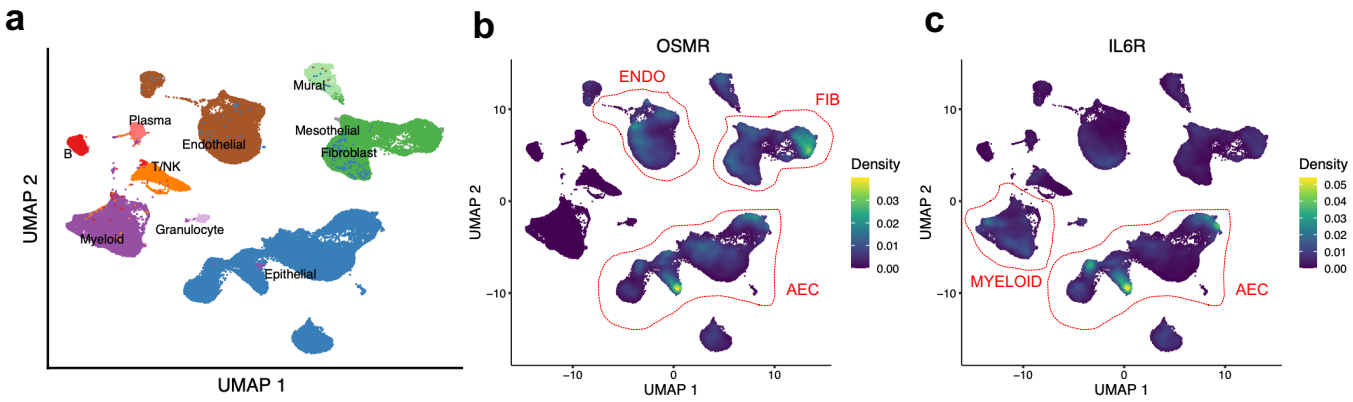

1450 **Extended data 7.**

1451 **Single cell transcriptional analysis of human ILD lung tissue.**

1452 a. UMAP showing cellular populations recovered from digested lung tissue.

1453 b. UMAP showing *OSMR* expression density across cells.

1454 c. UMAP showing *IL6R* expression density across cells.

Extended Data 8.

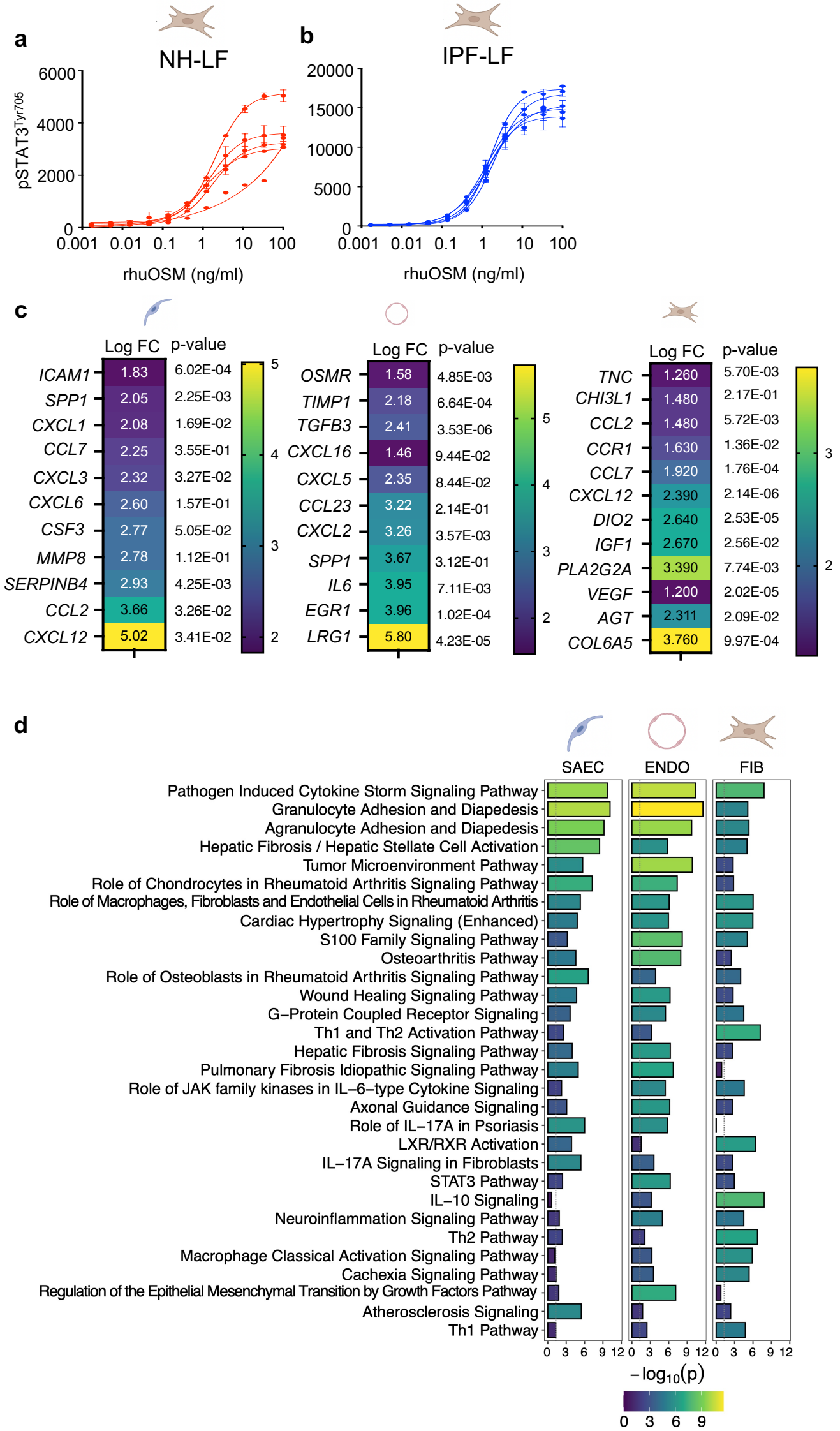

1455 **Extended data 8.**

1456 **OSM-driven pathways in disease-relevant cells.**

1457 a. Normal primary human lung FIB (NH-LF) were cultured, as described in
1458 methods, and stimulated with rhOSM at the indicated concentrations for 15
1459 mins. Cell lysates were recovered and $pSTAT3^{Tyr705}$ was measured by MSD.
1460 b. IPF-derived human lung FIB (IPF-LF) were cultured, as described in methods,
1461 and stimulated with rhOSM at the indicated concentrations for 15 mins. Cell
1462 lysates were recovered and $pSTAT3^{Tyr705}$ was measured by MSD.
1463 c. Primary human SAEC, ENDO or FIB were cultured, as described in methods,
1464 and stimulated with rhOSM (10ng/ml) for 24hrs. RNA was extracted for RNA
1465 seq analysis. Disease-relevant differentially expressed genes ($P<0.05$) are shown
1466 for each cell type. Log_2FC values shown in boxes with p-values shown to the
1467 right.
1468 d. Primary human SAEC, ENDO or FIB were cultured, as described in methods,
1469 and stimulated with rhOSM (10ng/ml) for 24hrs. Ingenuity pathways analysis
1470 (IPA) analyses of OSM-driven responses are shown for each cell type.

Extended Data 9.

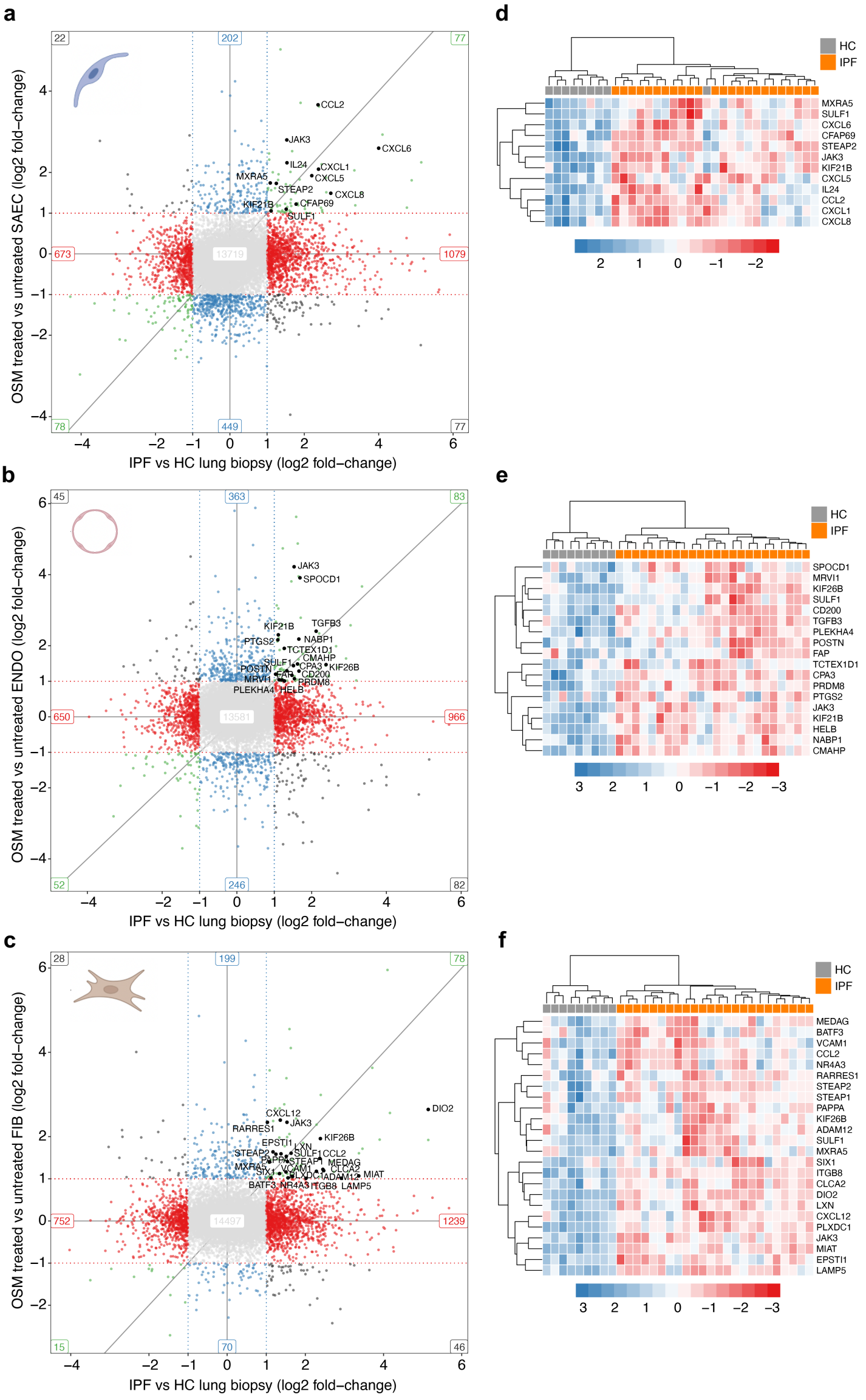

1471 **Extended data 9.**

1472 **Correlation between OSM-induced responses *in vitro* and observed responses in IPF**
1473 **and SSc-ILD lung tissue *ex vivo*.**

1474 Primary human SAEC (a), ENDO (b) or FIB (c) were cultured, as described in methods,
1475 and stimulated with rhOSM (10ng/ml) for 24hrs. These transcriptional responses are
1476 plotted against observed transcriptional responses in IPF lung tissue (left). The common
1477 genes identified between *in vitro* stimulated cells and *ex vivo* observed responses in IPF
1478 are then plotted in heatmaps for genes significantly upregulated in IPF (FDR $P<0.05$) to
1479 identify concordance between OSM-driven cell type specific response and upregulation
1480 in IPF lung tissue (d-f).

Extended Data 10.

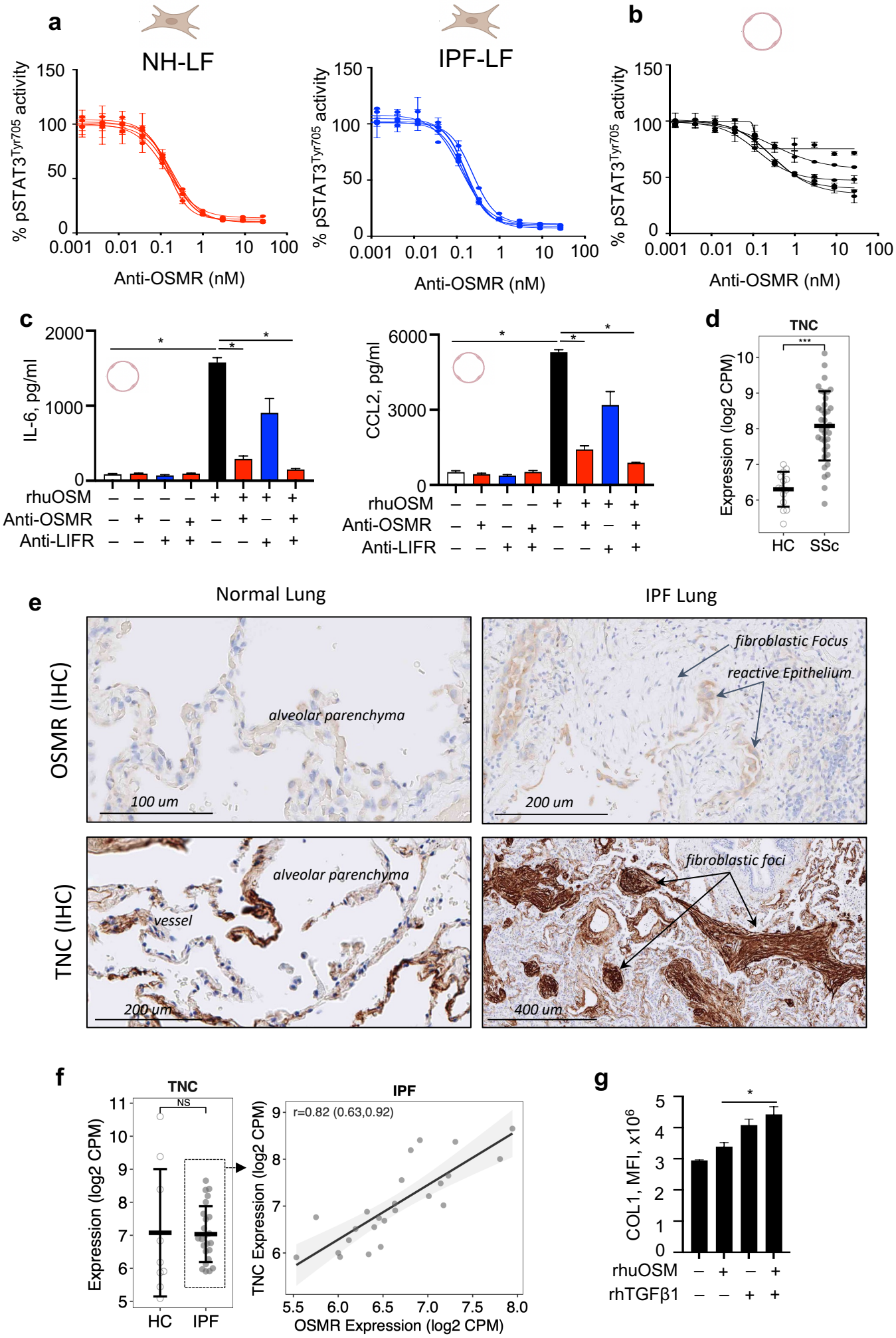

1481 **Extended data 10.**

1482 **OSMR-dependent activity of OSM in disease-relevant cells.**

1483 a. Normal primary human lung FIB (NH-LF) or IPF-derived human lung FIB (IPF-
1484 LF) were cultured, as described in methods, and stimulated with rhOSM
1485 (10ng/ml). Some cells were treated with anti-OSMR, at the indicated
1486 concentrations, from 120 mins prior to OSM treatment. Cell lysates were
1487 recovered and pSTAT3^{Tyr705} was measured by MSD. Data is expressed as % of
1488 remaining pSTAT3^{Tyr705}.

1489 b. Primary human ENDO cells were cultured, as described in methods and
1490 stimulated with rhOSM (10ng/ml). Some cells were treated with anti-OSMR, at
1491 the indicated concentrations, from 120 mins prior to OSM treatment. Cell lysates
1492 were recovered and pSTAT3^{Tyr705} was measured by MSD. Data is expressed as %
1493 of remaining pSTAT3^{Tyr705}.

1494 c. Primary human ENDO cells were cultured, as described in methods, and
1495 stimulated with rhOSM (10ng/ml) for 24hrs with anti-OSMR (50ug/ml) or anti-
1496 LIFR (50ug/ml) from 120 mins prior to OSM treatment and throughout. IL-6 and
1497 CCL2/MCP1 were measured by luminex in supernatants. P value calculated by
1498 t-test. Graphs show mean ± SD. * $P<0.05$.

1499 d. Skin biopsies obtained from healthy controls (n=14) and SSc patients (n=36),
1500 participating in the focuSSced clinical trial and *TNC* transcripts measured.
1501 Graphs show mean ± SD. *** FDR $P<0.0005$

1502 e. Normal human lung and IPF lung tissue was stained with anti-human OSMR or
1503 anti-human TNC. OSMR+ staining and TNC+ staining is shown.

1504 f. Lung biopsies were obtained from healthy controls (n=9) and IPF patients (n=24),
1505 RNA-seq was carried out and *TNC* transcripts analyzed (left). TNC levels were
1506 plotted against *OSMR* expression (right); linear fit, Pearson correlation, and 95%
1507 confidence interval is shown. Graphs show log_2 normalized CPM, mean ± SD. NS
1508 not significant

1509 g. Primary human FIB cells were cultured, as described in methods, and stimulated
1510 with rhOSM (10ng/ml) or rhTGFβ (1ng/ml), or both rhOSM and rhTGFβ for 72
1511 hrs. Collagen 1 (COL) secretion was stained and assessed using Cell Insight CX7,

1512 in the scar-in-a-jar assay, as described in methods. P value calculated by t-test.
1513 Graphs show mean ± SD. * $P<0.05$.

1514 # References

1515 1. Ley, B., Collard, H.R. & King, T.E., Jr. Clinical course and prediction of survival in
1516 idiopathic pulmonary fibrosis. *Am J Respir Crit Care Med* **183**, 431-440 (2011).
1517 2. Pope, J.E.*, et al.* Systemic Sclerosis and Associated Interstitial Lung Disease in Ontario,
1518 Canada: An Examination of Prevalence and Survival Over 10 Years. *J Rheumatol* **48**,
1519 1427-1434 (2021).
1520 3. Zheng, Q.*, et al.* Mortality and survival in idiopathic pulmonary fibrosis: a systematic
1521 review and meta-analysis. *ERJ Open Res* **8**(2022).
1522 4. Bouros, D.*, et al.* Histopathologic subsets of fibrosing alveolitis in patients with systemic
1523 sclerosis and their relationship to outcome. *Am J Respir Crit Care Med* **165**, 1581-1586
1524 (2002).
1525 5. De Lauretis, A.*, et al.* Serum interleukin 6 is predictive of early functional decline and
1526 mortality in interstitial lung disease associated with systemic sclerosis. *J Rheumatol* **40**,
1527 435-446 (2013).
1528 6. Saito, F.*, et al.* Role of interleukin-6 in bleomycin-induced lung inflammatory changes in
1529 mice. *Am J Respir Cell Mol Biol* **38**, 566-571 (2008).
1530 7. Kitaba, S.*, et al.* Blockade of interleukin-6 receptor alleviates disease in mouse model of
1531 scleroderma. *Am J Pathol* **180**, 165-176 (2012).
1532 8. Kobayashi, T.*, et al.* Bidirectional role of IL-6 signal in pathogenesis of lung fibrosis.
1533 *Respir Res* **16**, 99 (2015).
1534 9. Kang, S., Tanaka, T., Narazaki, M. & Kishimoto, T. Targeting Interleukin-6 Signaling in
1535 Clinic. *Immunity* **50**, 1007-1023 (2019).
1536 10. Khanna, D.*, et al.* Safety and efficacy of subcutaneous tocilizumab in adults with
1537 systemic sclerosis (faSScinate): a phase 2, randomised, controlled trial. *Lancet* **387**,
1538 2630-2640 (2016).
1539 11. Khanna, D.*, et al.* Tocilizumab in systemic sclerosis: a randomised, double-blind,
1540 placebo-controlled, phase 3 trial. *Lancet Respir Med* **8**, 963-974 (2020).
1541 12. King, T.E., Jr.*, et al.* A phase 3 trial of pirfenidone in patients with idiopathic pulmonary
1542 fibrosis. *N Engl J Med* **370**, 2083-2092 (2014).
1543 13. Richeldi, L.*, et al.* Efficacy and safety of nintedanib in idiopathic pulmonary fibrosis. *N*
1544 *Engl J Med* **370**, 2071-2082 (2014).
1545 14. Chen, C.H.*, et al.* The safety of nintedanib for the treatment of interstitial lung disease: A
1546 systematic review and meta-analysis of randomized controlled trials. *PLoS One* **16**,
1547 e0251636 (2021).
1548 15. Cottin, V.*, et al.* Long-term safety of pirfenidone: results of the prospective,
1549 observational PASSPORT study. *ERJ Open Res* **4**(2018).
1550 16. Henderson, N.C., Rieder, F. & Wynn, T.A. Fibrosis: from mechanisms to medicines.
1551 *Nature* **587**, 555-566 (2020).
1552 17. Levy, M.T., Trojanowska, M. & Reuben, A. Oncostatin M: a cytokine upregulated in
1553 human cirrhosis, increases collagen production by human hepatic stellate cells. *J Hepatol*
1554 **32**, 218-226 (2000).
1555 18. Scaffidi, A.K.*, et al.* Oncostatin M stimulates proliferation, induces collagen production
1556 and inhibits apoptosis of human lung fibroblasts. *Br J Pharmacol* **136**, 793-801 (2002).
1557 19. Stawski, L. & Trojanowska, M. Oncostatin M and its role in fibrosis. *Connect Tissue Res*
1558 **60**, 40-49 (2019).

1559 20. Mozaffarian, A., *et al.* Mechanisms of oncostatin M-induced pulmonary inflammation
1560 and fibrosis. *J Immunol* **181**, 7243-7253 (2008).
1561 21. Abe, H., *et al.* Macrophage hypoxia signaling regulates cardiac fibrosis via Oncostatin M.
1562 *Nat Commun* **10**, 2824 (2019).
1563 22. Matsuda, M., *et al.* Oncostatin M causes liver fibrosis by regulating cooperation between
1564 hepatic stellate cells and macrophages in mice. *Hepatology* **67**, 296-312 (2018).
1565 23. Ayaub, E.A., *et al.* Overexpression of OSM and IL-6 impacts the polarization of pro-
1566 fibrotic macrophages and the development of bleomycin-induced lung fibrosis. *Sci Rep* **7**,
1567 13281 (2017).
1568 24. Bamber, B., Reife, R.A., Haugen, H.S. & Clegg, C.H. Oncostatin M stimulates excessive
1569 extracellular matrix accumulation in a transgenic mouse model of connective tissue
1570 disease. *J Mol Med (Berl)* **76**, 61-69 (1998).
1571 25. Foglia, B., *et al.* Oncostatin M, A Profibrogenic Mediator Overexpressed in Non-
1572 Alcoholic Fatty Liver Disease, Stimulates Migration of Hepatic Myofibroblasts. *Cells*
1573 **9**(2019).
1574 26. Fritz, D.K., *et al.* A mouse model of airway disease: oncostatin M-induced pulmonary
1575 eosinophilia, goblet cell hyperplasia, and airway hyperresponsiveness are STAT6
1576 dependent, and interstitial pulmonary fibrosis is STAT6 independent. *J Immunol* **186**,
1577 1107-1118 (2011).
1578 27. Jengelley, D.H.A., *et al.* Exogenous Oncostatin M induces Cardiac Dysfunction,
1579 Musculoskeletal Atrophy, and Fibrosis. *Cytokine* **159**, 155972 (2022).
1580 28. Wong, S., Botelho, F.M., Rodrigues, R.M. & Richards, C.D. Oncostatin M
1581 overexpression induces matrix deposition, STAT3 activation, and SMAD1 Dysregulation
1582 in lungs of fibrosis-resistant BALB/c mice. *Lab Invest* **94**, 1003-1016 (2014).
1583 29. Fabre, T., *et al.* Identification of a broadly fibrogenic macrophage subset induced by type
1584 3 inflammation. *Sci Immunol* **8**, eadd8945 (2023).
1585 30. Ishida, Y., *et al.* Essential involvement of the CX3CL1-CX3CR1 axis in bleomycin-
1586 induced pulmonary fibrosis via regulation of fibrocyte and M2 macrophage migration.
1587 *Sci Rep* **7**, 16833 (2017).
1588 31. Okuma, T., *et al.* C-C chemokine receptor 2 (CCR2) deficiency improves bleomycin-
1589 induced pulmonary fibrosis by attenuation of both macrophage infiltration and production
1590 of macrophage-derived matrix metalloproteinases. *J Pathol* **204**, 594-604 (2004).
1591 32. Mauer, J., *et al.* Signaling by IL-6 promotes alternative activation of macrophages to
1592 limit endotoxemia and obesity-associated resistance to insulin. *Nat Immunol* **15**, 423-430
1593 (2014).
1594 33. Tiev, K.P., *et al.* Serum CC chemokine ligand-18 predicts lung disease worsening in
1595 systemic sclerosis. *Eur Respir J* **38**, 1355-1360 (2011).
1596 34. Ayaub, E.A., *et al.* IL-6 mediates ER expansion during hyperpolarization of alternatively
1597 activated macrophages. *Immunol Cell Biol* **97**, 203-217 (2019).
1598 35. Effenberger, M., *et al.* Interleukin-11 drives human and mouse alcohol-related liver
1599 disease. *Gut* **72**, 168-179 (2023).
1600 36. Ng, B., *et al.* Interleukin-11 is a therapeutic target in idiopathic pulmonary fibrosis. *Sci*
1601 *Transl Med* **11**(2019).
1602 37. Ng, B., *et al.* Fibroblast-specific IL11 signaling drives chronic inflammation in murine
1603 fibrotic lung disease. *FASEB J* **34**, 11802-11815 (2020).

1604 38. Schafer, S., *et al.* IL-11 is a crucial determinant of cardiovascular fibrosis. *Nature* **552**,
1605 110-115 (2017).
1606 39. Chen, Q., *et al.* IL-11 receptor alpha in the pathogenesis of IL-13-induced inflammation
1607 and remodeling. *J Immunol* **174**, 2305-2313 (2005).
1608 40. Lee, C.G., *et al.* Endogenous IL-11 signaling is essential in Th2- and IL-13-induced
1609 inflammation and mucus production. *Am J Respir Cell Mol Biol* **39**, 739-746 (2008).
1610 41. Minshall, E., *et al.* IL-11 expression is increased in severe asthma: association with
1611 epithelial cells and eosinophils. *J Allergy Clin Immunol* **105**, 232-238 (2000).
1612 42. Tang, W., *et al.* Targeted expression of IL-11 in the murine airway causes lymphocytic
1613 inflammation, bronchial remodeling, and airways obstruction. *J Clin Invest* **98**, 2845-
1614 2853 (1996).
1615 43. Zhu, M., *et al.* IL-11 Attenuates Liver Ischemia/Reperfusion Injury (IRI) through STAT3
1616 Signaling Pathway in Mice. *PLoS One* **10**, e0126296 (2015).
1617 44. Tan, Y., *et al.* IL11-mediated stromal cell activation may not be the master regulator of
1618 pro-fibrotic signaling downstream of TGFbeta. *Front Immunol* **15**, 1293883 (2024).
1619 45. Huguier, V., *et al.* Oncostatin M exerts a protective effect against excessive scarring by
1620 counteracting the inductive effect of TGFbeta1 on fibrosis markers. *Sci Rep* **9**, 2113
1621 (2019).
1622 46. Xu, P., *et al.* Oncostatin M/Oncostatin M Receptor Signal Induces Radiation-Induced
1623 Heart Fibrosis by Regulating SMAD4 in Fibroblast. *Int J Radiat Oncol Biol Phys* (2023).
1624 47. Zhang, X., *et al.* OSM Enhances Angiogenesis and Improves Cardiac Function after
1625 Myocardial Infarction. *Biomed Res Int* **2015**, 317905 (2015).
1626 48. Headland, S.E., *et al.* Oncostatin M expression induced by bacterial triggers drives
1627 airway inflammatory and mucus secretion in severe asthma. *Sci Transl Med* **14**, eabf8188
1628 (2022).
1629 49. Bhattacharyya, S., *et al.* Tenascin-C drives persistence of organ fibrosis. *Nat Commun* **7**,
1630 11703 (2016).
1631 50. Choi, J., *et al.* Inflammatory Signals Induce AT2 Cell-Derived Damage-Associated
1632 Transient Progenitors that Mediate Alveolar Regeneration. *Cell Stem Cell* **27**, 366-382
1633 e367 (2020).
1634 51. Wang, L., *et al.* Serum Proteomics Identifies Biomarkers Associated With the
1635 Pathogenesis of Idiopathic Pulmonary Fibrosis. *Mol Cell Proteomics* **22**, 100524 (2023).
1636 52. Maher, T.M., *et al.* Safety, tolerability, pharmacokinetics, and pharmacodynamics of
1637 GLPG1690, a novel autotaxin inhibitor, to treat idiopathic pulmonary fibrosis (FLORA):
1638 a phase 2a randomised placebo-controlled trial. *Lancet Respir Med* **6**, 627-635 (2018).
1639 53. Ohkura, S.I., *et al.* Augmented sphingosine 1 phosphate receptor-1 signaling in cardiac
1640 fibroblasts induces cardiac hypertrophy and fibrosis through angiotensin II and
1641 interleukin-6. *PLoS One* **12**, e0182329 (2017).
1642 54. Denton, C.P., *et al.* Biological and clinical insights from a randomized phase 2 study of
1643 an anti-oncostatin M monoclonal antibody in systemic sclerosis. *Rheumatology (Oxford)*
1644 **62**, 234-242 (2022).
1645 55. Sofen, H., *et al.* Efficacy and safety of vixarelimab, a human monoclonal oncostatin M
1646 receptor beta antibody, in moderate-to-severe prurigo nodularis: a randomised, double-
1647 blind, placebo-controlled, phase 2a study. *EClinicalMedicine* **57**, 101826 (2023).

1648 56. Marden, G., *et al.* The role of the oncostatin M/OSM receptor beta axis in activating
1649 dermal microvascular endothelial cells in systemic sclerosis. *Arthritis Res Ther* **22**, 179
1650 (2020).
1651 57. Chakraborty, D., *et al.* Activation of STAT3 integrates common profibrotic pathways to
1652 promote fibroblast activation and tissue fibrosis. *Nat Commun* **8**, 1130 (2017).
1653 58. Carey, W.A., Taylor, G.D., Dean, W.B. & Bristow, J.D. Tenascin-C deficiency attenuates
1654 TGF-ss-mediated fibrosis following murine lung injury. *Am J Physiol Lung Cell Mol*
1655 *Physiol* **299**, L785-793 (2010).
1656 59. Meng, X.M., Nikolic-Paterson, D.J. & Lan, H.Y. TGF-beta: the master regulator of
1657 fibrosis. *Nat Rev Nephrol* **12**, 325-338 (2016).
1658 60. Sarkozi, R., *et al.* Oncostatin M inhibits TGF-beta1-induced CTGF expression via
1659 STAT3 in human proximal tubular cells. *Biochem Biophys Res Commun* **424**, 801-806
1660 (2012).
1661 61. Sarkozi, R., *et al.* Oncostatin M is a novel inhibitor of TGF-beta1-induced matricellular
1662 protein expression. *Am J Physiol Renal Physiol* **301**, F1014-1025 (2011).
1663 62. de Almeida, A.R., *et al.* Increased levels of the soluble oncostatin M receptor (sOSMR)
1664 and glycoprotein 130 (sgp130) in systemic sclerosis patients and associations with
1665 clinical parameters. *Immunobiology* **225**, 151964 (2020).
1666 63. Diveu, C., *et al.* Molecular and functional characterization of a soluble form of oncostatin
1667 M/interleukin-31 shared receptor. *J Biol Chem* **281**, 36673-36682 (2006).
1668 64. George, P.M., *et al.* Progressive fibrosing interstitial lung disease: clinical uncertainties,
1669 consensus recommendations, and research priorities. *Lancet Respir Med* **8**, 925-934
1670 (2020).
1671 65. Raghu, G., *et al.* CC-chemokine ligand 2 inhibition in idiopathic pulmonary fibrosis: a
1672 phase 2 trial of carlumab. *Eur Respir J* **46**, 1740-1750 (2015).
1673 66. Widjaja, A.A., *et al.* Redefining IL11 as a regeneration-limiting hepatotoxin and
1674 therapeutic target in acetaminophen-induced liver injury. *Sci Transl Med* **13**(2021).
1675 67. Widjaja, A.A., *et al.* Inhibiting Interleukin 11 Signaling Reduces Hepatocyte Death and
1676 Liver Fibrosis, Inflammation, and Steatosis in Mouse Models of Nonalcoholic
1677 Steatohepatitis. *Gastroenterology* **157**, 777-792 e714 (2019).
1678 68. Fung, K.Y., *et al.* Emerging roles for IL-11 in inflammatory diseases. *Cytokine* **149**,
1679 155750 (2022).
1680 69. Amati, F., *et al.* Lung Microbiome in Idiopathic Pulmonary Fibrosis and Other Interstitial
1681 Lung Diseases. *Int J Mol Sci* **23**(2022).
1682 70. Chioma, O.S., *et al.* Gut microbiota modulates lung fibrosis severity following acute lung
1683 injury in mice. *Commun Biol* **5**, 1401 (2022).
1684 71. Botelho, F.M., *et al.* Pulmonary expression of oncostatin M (OSM) promotes inducible
1685 BALT formation independently of IL-6, despite a role for IL-6 in OSM-driven
1686 pulmonary inflammation. *J Immunol* **191**, 1453-1464 (2013).
1687 72. Moss, B.J., Ryter, S.W. & Rosas, I.O. Pathogenic Mechanisms Underlying Idiopathic
1688 Pulmonary Fibrosis. *Annu Rev Pathol* **17**, 515-546 (2022).
1689 73. Noble, P.W. Epithelial fibroblast triggering and interactions in pulmonary fibrosis.
1690 *European Respiratory Review* **17**, 123-129 (2008).
1691 74. Sakai, N. & Tager, A.M. Fibrosis of two: Epithelial cell-fibroblast interactions in
1692 pulmonary fibrosis. *Biochim Biophys Acta* **1832**, 911-921 (2013).

1693 75. Clynick, B., *et al.* Biomarker signatures for progressive idiopathic pulmonary fibrosis.
1694 *Eur Respir J* **59**(2022).
1695 76. Gao, X., *et al.* Osteopontin Links Myeloid Activation and Disease Progression in
1696 Systemic Sclerosis. *Cell Rep Med* **1**, 100140 (2020).
1697 77. Pardo, A., *et al.* Up-regulation and profibrotic role of osteopontin in human idiopathic
1698 pulmonary fibrosis. *PLoS Med* **2**, e251 (2005).
1699 78. Garcia, A.N., *et al.* eNAMPT Is a Novel Damage-associated Molecular Pattern Protein
1700 That Contributes to the Severity of Radiation-induced Lung Fibrosis. *Am J Respir Cell*
1701 *Mol Biol* **66**, 497-509 (2022).
1702 79. Bhattacharyya, S., Midwood, K.S. & Varga, J. Tenascin-C in fibrosis in multiple organs:
1703 Translational implications. *Semin Cell Dev Biol* **128**, 130-136 (2022).
1704 80. Li, J., *et al.* CD3 bispecific antibody-induced cytokine release is dispensable for cytotoxic
1705 T cell activity. *Sci Transl Med* **11**(2019).
1706 81. Decaris, M.L., *et al.* Proteomic analysis of altered extracellular matrix turnover in
1707 bleomycin-induced pulmonary fibrosis. *Mol Cell Proteomics* **13**, 1741-1752 (2014).
1708 82. Nlandu Khodo, S., *et al.* NADPH-oxidase 4 protects against kidney fibrosis during
1709 chronic renal injury. *J Am Soc Nephrol* **23**, 1967-1976 (2012).
1710 83. Good, R.B., *et al.* A high content, phenotypic 'scar-in-a-jar' assay for rapid quantification
1711 of collagen fibrillogenesis using disease-derived pulmonary fibroblasts. *BMC Biomed*
1712 *Eng* **1**, 14 (2019).
1713 84. Buechler, M.B., *et al.* A Stromal Niche Defined by Expression of the Transcription
1714 Factor WT1 Mediates Programming and Homeostasis of Cavity-Resident Macrophages.
1715 *Immunity* **51**, 119-130 e115 (2019).
1716 85. Team, R.C. R: A language and environment for statistical computing. R Foundation for
1717 Statistical Computing, Vienna, Austria. .
1718 86. Stuart, T., *et al.* Comprehensive Integration of Single-Cell Data. *Cell* **177**, 1888-1902
1719 e1821 (2019).
1720